Effect of parachute and airbag in reducing safety risk posed by small UAS to people on the ground

Jiang, Chengpeng; Blom, Henk; Rattanagraikanakorn, Borrdephong

DOI
10.1016/j.trip.2025.101521

Publication date
2025

Document Version
Final published version

Published in
Transportation Research Interdisciplinary Perspectives

Transportation Research Interdisciplinary Perspectives 32 (2025) 101521

Contents lists available at ScienceDirect

Transportation Research Interdisciplinary Perspectives

journal homepage: www.sciencedirect.com/journal/transportation-research-interdisciplinary-perspectives

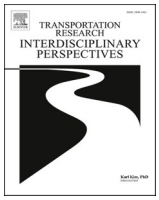

Effect of parachute and airbag in reducing safety risk posed by small UAS to people on the ground

Chengpeng Jiang [a,b,*], Henk Blom [b], Borrdephong Rattanagraikanakorn [c]

[a] Integrated Transportation Big Data Research Center, Hangzhou Innovative Institution of Beihang University, Hangzhou, China
[b] Faculty of Aerospace Engineering, Delft University of Technology, Delft, the Netherlands
[c] International School of Engineering, Chulalongkorn University, Bangkok, Thailand

ARTICLE INFO

Keywords:
Unmanned Aircraft Systems
Third Party Risk
Parcel delivery
Dynamical simulation
Fatality risk

ABSTRACT

To reduce the safety risk posed by small Unmanned Aircraft System (UAS) to persons on the ground, one of the mitigating measures is to equip the UAS with an airbag in combination with a parachute, both of which are deployed in case of an uncontrolled descent. In literature, methods for the evaluation of the effect of a parachute alone have been developed. This paper develops a method to assess the safety risk for persons on the ground posed by a UAS that is both equipped with an airbag and a parachute. For the descent phase of the UAS to the ground, existing models are used. The novel part is the dynamical simulation of the effect on a human body of impact and interaction of a UAS with airbag. For the human impact simulation, use is made of Multi Body System (MBS) model for the UAS and the human; in combination with Finite Element (FE) model of the airbag. This method is applied for a specific parcel delivery UAS, of 15 kg weigh, for cases with and without airbag. The results obtained show that the combination of parachute and airbag can reduce the safety risk posed to people on the ground by more than one order in magnitude. Comparison with existing models for parachute alone, show that the novel method is much better in taking UAS design and material properties into account. The paper also shows that the dynamical simulation results obtained provide effective feedback to the further improvement of the airbag design.

1. Introduction

The use of Unmanned Aircraft System (UAS) [ICAO, 2011] is of high interest for services like medical aid, surveillance, parcel delivery and air taxi. As has been identified in [EASA, 2021], the advantages of commercial UAS-based services may come with negative issues for overflown population. One of the main negative issues identified is ground Third Party Risk (TPR), i.e. the safety risk posed by UAS flights to people and property on the ground [Clothier et al., 2018]. The development of these commercial UAS-based services encounters a yet unresolved gap: many potential customers live in urban and metropolitan areas where these issues play a key role. In line with this, standing safety regulations typically consider UAS not (yet) safe enough to be allowed to fly to potential customers in urban areas [FAA, 2016; JARUS, 2022, 2023].

Relevant tactical measures in reducing the TPR effect of an uncontrolled descent are of three complementary types: i) Improvements of the physical UAS design; ii) Deployment of a parachute to reduce the ground crash speed [DJI, 2022; Flyfire, 2022; Antwork, 2020]; and iii) Equipping a UAS with a deployable airbag [Cawthorne, 2016; Disney, 2016; DJI, 2019; Manta Air, 2023; SAES, 2025]. A complementary role in these design directions is played by the application of ground TPR assessment to a UAS design, and to feedback the assessment results to further improve the design.

The commonly adopted indicator for ground TPR per UAS flight hour is the expected number of ground fatalities. In literature, e.g. [Clothier et al., 2007; Melnyk et al., 2014; Bertrand et al., 2017; Washington et al., 2017], the common model for this indicator reads as:

$$\mathbb{E}\{n_F\} = \lambda_{system} \cdot \rho_{population} \cdot (1 - P_{shelter}) \cdot A_{impact} \cdot \mathbb{P}\{F|impact\} \tag{1.1}$$

where n_F denotes the number of ground fatalities per flight hour, λ_{system} is the ground crash event rate per flight hour of the UAS, $\rho_{population}$ is the population density of the overflown area, $P_{shelter}$ is the probability that a

* Corresponding author at: Integrated transportation big data research center, Hangzhou Innovative Institution of Beihang University, No. 99 Changhe Street, Hangzhou, China.
E-mail address: jcp1020@outlook.com (C. Jiang).

https://doi.org/10.1016/j.trip.2025.101521
Received 8 August 2023; Received in revised form 19 June 2025; Accepted 1 July 2025
Available online 9 July 2025

person on the ground is sheltered to the crashing UAS, A_{impact} is the size of the "crash impact area" on the ground, and $\mathbb{P}\{F|impact\}$ is the conditional probability of Fatality (PoF), given the UAS crashes, and there is one person in the "crash impact area".

Of the five terms in equation (1.1), three are influenced by the UAS design, i.e. λ_{system}, A_{impact} and $\mathbb{P}\{F|impact\}$, the latter two of which play a key role in evaluating the effect of equipping a drone with an airbag and a parachute. Therefore, the remainder of this paper focuses on the product $A_{impact}\bullet\mathbb{P}\{F|impact\}$.

As is shown in overviews by [Melnyk et al., 2014; Washington et al., 2017; Blom et al., 2021], in literature multiple parametric models for A_{impact} and $\mathbb{P}\{F|impact\}$ have been developed that apply to a wide variety of UAS types. This way the effect of parachute deployment on A_{impact} and $\mathbb{P}\{F|impact\}$ has also been studied [Bertrand et al., 2017; la Cour-Harbo, 2019]. One shortcoming of these parametric models is their large variety, as a result of which there is a significant range of possible values, both for A_{impact} and for $\mathbb{P}\{F|impact\}$.

To improve this situation, a complementary development is to replace a parametric model for $\mathbb{P}\{F|impact\}$ by a dynamical simulation of a Finite-Element (FE) or a Multi-Body-System (MBS) model of a specific UAS collision with a human body [Koh et al., 2018; Arterburn et al, 2019; Rattanagraikanakorn et al., 2019, 2020, 2021; Weng et al., 2021]. The basis for this dynamical modelling and simulation approach stems from car crash research in automotive industry, where dynamical simulation of collision effect on human body and capturing this in injury and fatality levels is a well-developed topic. As a result of this research, dynamical simulation models have been developed and validated for collisions involving human and human crash dummies that are used in car crash testing. Examples of well-developed and validated simulation platforms are: [THUMS, 2018] and [MADYMO, 2017a, b]. The former makes use of FE models of human body involved in a car collision, while the latter makes use of MBS models. Dynamic simulation of a collision yields detailed acceleration curves over time of various parts of the human body involved. These results are subsequently translated into well-developed injury scales. The commonly used injury scales are Head Injury Criteria (HIC), Neck Injury Criteria (Nij) and Viscous Criteria (VC) for injuries to head, neck and other body parts respectively. HIC takes the effect of sudden head acceleration into account [Hutchinson et al., 1998; Schmitt et al., 2019]. Nij considers the consequences of head movements on neck forces and moments [Klinich et al., 1996; Parr et al., 2012]. VC considers that injury to soft tissue injury is compression and rate dependent [Lau and Viano, 1986; Viano et al. 1989].

For dynamical simulation of UAS collision with a human body, a validated model of the UAS type considered has to be developed and integrated in one of these platforms. In addition, there is need for a transformation of assessed injury levels to probability of fatality. FE models have been developed by [Arterburn et al., 2019, Annex B] of UAS types: DJI Phantom III, Sensefly eBee+ and Precision Hawk MK III, for integration in the THUMS platform. [Weng et al., 2021] developed and integrated an FE model of DJI Phantom III in [THUMS, 2018]. [Rattanagraikanakorn et al., 2019, 2020, 2021] developed an MBS model of DJI Phantom III and integrated this in the MADYMO platform [MADYMO, 2017a,b], and models for the mapping of various injury scales to Probability of Fatality. These dynamical simulation models have been validated through comparisons with acceleration measurements from laboratory controlled DJI Phantom III impact on human cadavers [Stark et al., 2019]. These comparisons have shown that simulations of FE and MBS models for DJI Phantom III impact on a human body, are remarkably accurate in assessing the effects of the UAS design and material, as well as the hitting location on the human body.

Although this dynamical modelling and simulation approach yields a more accurate assessment of $\mathbb{P}\{F|impact\}$, for the assessment of A_{impact} the only option is to adopt a parametric model, which yields a range of possible values. To improve this situation, [Jiang et al., 2024] have extended the dynamical modelling and simulation approach for the assessment of the product $A_{impact}\bullet\mathbb{P}\{F|impact\}$. As the key to this extension, [Jiang et al., 2024] have shown that $A_{impact}\bullet\mathbb{P}\{F|impact\}$ is equal to an integration of probability of human fatality over all possible offsets between centre locations of human and crashing UAS. [Jiang et al., 2024] have demonstrated that for a DJI Phantom III, this novel approach avoids the large range of possible values for $A_{impact}\bullet\mathbb{P}\{F|impact\}$ when adopting parametric models for A_{impact}.

The research objective of the current paper is to apply both the existing dynamical modelling and simulation method and the novel method of [Jiang et al., 2024] to the assessment of the product $A_{impact}\bullet\mathbb{P}\{F|impact\}$ for a small parcel delivery UAS that is equipped with deployable parachute and airbag, and to feedback the findings to the UAS design. To realize this objective, the research activities are:

i. To select the parcel delivery UAS with deployable parachute and airbag, and to evaluate parametric models to assess A_{impact} and $\mathbb{P}\{F|impact\}$;
ii. To develop the dynamical simulation models to assess $A_{impact}\bullet\mathbb{P}\{F|impact\}$ for the selected UAS;
iii. To conduct dynamical model simulations for three UAS cases: A (with parachute and airbag); B (with parachute only); C (without parachute/airbag), and to compare the results from the existing and the novel approaches;
iv. To feedback the results obtained to the design; and apply the novel dynamical modelling and simulation to an improved design.

During activity i, the RA3 UAS design of [Antwork, 2023] has been selected, and the existing parametric models are applied for TPR assessment. During activity ii, use is made of FE modelling and dynamical simulation of an airbag in combination with an MBS model of UAS impacting on a human body [Happee et al., 2003; MADYMO, 2023]. During activity iii, the developed MBS and FE models are simulated for cases A, B and C, and a comparison is made of the results obtained by the novel method versus the existing method, i.e. combining a parametric model for A_{impact} with dynamical simulation for $\mathbb{P}\{F|impact\}$. During activity iv, the airbag design has been improved to better mitigate remaining risks, and a second dynamical modelling and simulation cycle is conducted.

The paper is organized as follows. Section 2 provides the background of existing ground TPR assessment methods, and conducts activity i. Section 3 conducts activity ii, by developing the MBS and FE models for the RA3 UAS with airbag, and a model to accumulate various assessed injury levels to $\mathbb{P}\{F|impact\}$. Section 4 explains the novel method of [Jiang et al., 2024] in assessing the product $A_{impact}\bullet\mathbb{P}\{F|impact\}$. Section 5 conducts simulations with the dynamical model from section 3 according to the method of section 4, and compares the results to those using a parametric model for A_{impact}. Section 6 uses the results from section 5 to conduct a second cycle of dynamical modelling and simulation of an improved airbag design. Section 7 draws conclusions.

2. Selection of UAS under design, and evaluation of parametric models

This section applies existing ground TPR assessments methods to a selected parcel delivery UAS under design, without airbag. Subsection 2.1 starts with a specification of the RA3 UAS under design. Subsection 2.2 assesses the descent velocities for RA3 with deployed parachute (case B), and without (case C). Subsection 2.3 gives an overview of parametric models for the assessment of A_{impact} and $\mathbb{P}\{F|impact\}$. Subsection 2.4 assesses A_{impact} and $\mathbb{P}\{F|impact\}$ for cases B and C of the RA3 UAS under design.

2.1. The parcel delivery UAS under design

The specific parcel delivery UAS to be considered is the RA3 design of [Antwork, 2023], which is depicted in Fig. 1a. As shown in Fig. 1b, the RA3 UAS has a deployable parachute for uncontrolled descent, which reduces the RA3 descent velocity at impact. In addition, the RA3 cargo box has foam at its bottom to further reduce effect of impact on a human. Specifications of the RA3 UAS are given in Table 1.

The parachute system is embedded at the top of the RA3 mainframe [Antwork, 2020], and consists of a parachute, a parachute box, a canopy, and a gas trigger. As shown in Fig. 1b, four ropes connect four corners of the expanded parachute to four corners of the parachute carrying box part of the RA3 UAS. Distance between nearby parachute corners is 1.65 m. During descent, the parachute decelerates the descending velocity and helps the UAS to keep an upright attitude to land with its bottom touching the ground. Under conditions of side wind, the parachute–drone system tends to match the wind's horizontal speed, at which state the drone hangs in a near-vertical line beneath the parachute. A variation of side wind may cause oscillation of the parachute, but with much smaller influence on the drone body due to its symmetrical and streamlined shape. Hence, for the impact modelling, it is assumed that a deployed parachute reduces the impact velocity, though does not play a further role during human impact, and that the UAS touches ground with an upright attitude.

2.2. Model based assessment of descent velocity

For the modelling of descent to the ground by a failing UAS, there are analytical models [la Cour-Harbo, 2020], and dynamical simulation models, including ballistic descent models with and without parachute [la Cour-Harbo, 2019] and high fidelity models without parachute [Forster and Hartman, 2017; Sun and Visser, 2019]. To align with [la Cour-Harbo, 2019], the following ballistic descent model is adopted:

$$\dot{s}_t = v_t \tag{2.1}$$

$$v_t = Col[0, 0, g] - \frac{1}{2}(A_S^d C_D^d + A_S^p C_D^p)\|v_t - w_t\|(v_t - w_t)\rho/m \tag{2.2}$$

where s_t is the UAS 3D position at moment t, v_t and w_t are the UAS 3D ground velocity and 3D wind velocity at moment t, g is gravitational constant, C_D^d and C_D^p are the drag coefficient of drone and parachute respectively, A_S^d and A_S^p are the reference surface areas of the drone and parachute respectively, ρ is air density, m is mass of the system. $A_S^p = 0$ if the parachute is not deployed.

Two types of descents are considered: descent of RA3 UAS with parachute, and descent of RA3 without parachute, i.e. $A_S^p = 0$. The RA3 relevant parameter values for Eq. (2.2) are shown in Table 1. Drag coefficient C_D^d and C_D^p are obtained through Computational Fluid Dynamics analysis of RA3 UAS and parachute for angle of attack 90 degrees (i.e. vertical descent with 0 degrees of pitch).

Table 1
Specifications of RA3 UAS with deployed parachute.

Parameter	Definition	Value
A_S^d	Reference area of RA3 drone	0.12 m^2
A_S^p	Reference area of parachute	2.72 m^2
C_D^d	Drag coefficient of RA3 drone	0.73
C_D^p	Drag coefficient of parachute	1.54
m	Mass of RA3 drone	15.0 kg
ρ	Air density	1.23 kg/m^3
g	Gravitational constant	9.81 m/s^2

For case B (RA3 with parachute, no airbag) and case C (RA3 without parachute/airbag), simulations of (2.1–2.2) are conducted for a UAS that starts to descent due to a failure at an altitude of 120 m under horizontal wind speed ranging from 0 to 10 m/s. The modelling parameters from Table 1 are used for descent simulations. It is worth noting that the parameters uncertainties (for wind speed, air density, etc.) are not considered, as the uncertainties have quite little influence on the outcomes of descent simulations.

In both cases, during descent, the attitude of UAS is assumed to be the same; i.e. pitch $\theta_{pitch} = 0^\circ$, roll $\theta_{roll} = 0^\circ$, yaw $\theta_{yaw} = 0^\circ$. The resulting impact velocities and descent angles are shown in Table 2.

For case C, the results in Table 2 show that the influence of wind on impact velocity is negligible. The influence on descend angle is also quite limited, varying from $\psi = 90^\circ$ for zero wind to $\psi = 84.7^\circ$ for 10 m/s wind. However, for case B, the results in Table 2 show that due to the

Table 2
Descent simulation results for cases B (parachute only) and C (no parachute, no airbag).

Wind velocity (m/s)	Case B		Case C	
	Impact velocity $\|v\|$ (m/s)	Descent angle ψ(degrees)	Impact velocity $\|v\|$ (m/s)	Descent angle ψ(degrees)
0	7.5	90.0	40.6	90.0
2	7.8	75.1	40.6	89.0
4	8.5	62.0	40.6	88.0
6	9.6	51.5	40.5	86.9
8	11.0	43.3	40.5	85.8
10	12.5	37.0	40.4	84.7

a. RA3 with parachute system embedded **b.** RA3 with parachute deployed.

Fig. 1. RA3 UAS.

drag of parachute, the impact velocities and the descent angles are significantly lower than in case C, though these values change under increasing horizontal wind.

2.3. Parametric model-based assessment of $\boldsymbol{A_{impact}}$ and $\mathbb{P}\{\boldsymbol{F}|\boldsymbol{impact}\}$ for RA3 cases B and C

This subsection applies parametric models of A_{impact} and $\mathbb{P}\{F|impact\}$ for RA3 cases B (parachute, no airbag) and C (no parachute, no airbag). For A_{impact} these are Gliding area model [RCC, 2001], Planform area model [Weibel and Hansman, 2004], and Maximum Take Off Weight (MTOW) based area model [Ale and Piers, 2000]. For $\mathbb{P}\{F|impact\}$ the parametric models are Range Commanders Council (RCC) model [RCC, 2001], Blunt Criteria (BC) model [Magister, 2010] and the Area Weight Kinetic Energy (AWKE) model [Arterburn, 2017]. Details of these parametric models is provided in Appendix D. The results obtained by applying these parametric models to RA3 cases B and C are collected in Table 3.

Evaluation of both the AWKE and the BC model for RA3 UAS weight of 15 kg and impact velocities in Table 2, yields $\mathbb{P}\{F|impact\} = 1$, both for case B and case C.

For crash impact area A_{impact}, the planform area model [Weibel and Hansman, 2004] adopts $A_{impact} = Width_{UAS} \times Length_{UAS}$; for RA3 UAS this equals $A_{impact} = 1.43m^2$ $(1.1m \times 1.3m)$. The Gliding area model [RCC, 2001] also takes the UAS descend angle and the size of human (height $1.73m$, diameter $0.2m$) into account; for RA3 UAS this yields $A_{impact} = 2.55m^2$ at descent angle of 90 degrees for no wind condition. Under 10 m/s horizontal wind: $A_{impact} = 6.45m^2$ at a descend angle of 37 degrees (case B) and $A_{impact} = 2.81m^2$ at a descend angle of 85 degrees (case C). The MTOW based area satisfies [Ale and Piers, 2000]: $A_{impact} = c_{Fit} \times m_{MTOW}$, with $m_{MTOW} = 15kg$, and the statistically fitted coefficient value $c_{Fit} = 0.2$ m^2/kg; for RA3 UAS this yields $A_{impact} = 3.00m^2$.

The results in Table 3 show that under zero wind, the $A_{impact} \bullet \mathbb{P}\{F|impact\}$ assessed values are the same for cases B and C. This confirms that for the RA3 UAS, the parametric models fall short to properly assess the mitigating effect of parachute and foam at the bottom of the RA3 cargo box. Under 10 m/s wind, the gliding area model-based assessment would imply that the effect of human impact is even larger for case B than it is for case C. These disappointing results for cases B and C form an extra motivation to develop dynamical modelling and simulation for the assessment of the effect of RA3 impact on a human.

3. Dynamical and injury risk models for an RA3 UAS with airbag hitting a human

This section develops RA3 dynamical and injury risk models for hitting a human by an RA3 UAS with a deployed airbag. Subsection 3.1 develops an MBS model for RA3 without airbag. Subsection 3.2 develops an FE model of the airbag, and its connection in the MBS model. Subsection 3.3 develops, for three injury types, the contact model with an existing MBS model for a male human body. Subsection 3.4 develops a model to accumulate the assessed injury levels into a single probability of human fatality.

Table 3
Parametric model-based assessments of A_{impact} and $\mathbb{P}\{F|impact\}$ for cases B (parachute only) and C (no parachute, no airbag).

	$\mathbb{P}\{F\|impact\}$	A_{impact}			
Case	AWKE or BC	Planform	MTOW	Gliding 0 m/s wind	Gliding 10 m/s wind
B	100 %	1.43 m^2	3.00 m^2	2.55 m^2	6.45 m^2
C	100 %	1.43 m^2	3.00 m^2	2.55 m^2	2.81 m^2

2.1. MBS model of RA3 UAS without airbag

The first step in MBS model development is the identification of the lumped mass rigid bodies that hold a significant portion of momentum in the system. In the actual RA3 UAS system depicted in Fig. 1, the main fuselage and each of the motor arms can be regarded as lumped masses. These can be modelled as distinct bodies within the MBS model. Certain details such as propellers or surface details are neglected, and these contribute insignificantly to the overall mass of the system and the propellers are assumed to be fully stopped during the crash.

The developed MBS model of the RA3 UAS is shown in Fig. 2. In summary, the MBS model consists of seven such bodies, one for the main body and one for each of the six arms. The main body includes the mainframe, cargo box, avionic system and battery that are lumped into Body 0. Motors at the end of each arm are lumped into Bodies 1–6. Universal joint type (2 degrees of freedom) is used to connect each motor arm to the main body – this allows rotational motion of the arms about the lateral and vertical axis. In the MBS model, each of these seven bodies is a rigid body, the shape of which is defined by a set of ellipsoid surfaces. The latter enables MBS contact detection and MBS contact effect evaluation. Details of the developed MBS model for the RA3 UAS are presented in Appendix A.

Per local body it is assumed that there is no breakage of any body part during impact. During impact, bending deformation on arms of RA3 UAS is determined by the torsional stiffness of the arm joint. The stiffness of the arm joints is obtained through quasi-static compression test of the RA3 UAS body. Details of the compression test and stiffness curve of arms are presented in Appendix A.

As shown in Fig. 3, the RA3 UAS consists of two types of materials. The main frame and drone arms are made from carbon fibre. The cargo box on bottom of the UAS is made from EPP foam.

2.2. Finite element (FE) model of airbag

As shown in Fig. 4, in the design to be evaluated, on the bottom of the drone an airbag is placed that, in deployed state, covers the bottom area of the mainframe. In normal operating conditions, the airbag is folded in the mainframe. During an emergency parachute descent, the airbag will be fully inflated. In the airbag system designed by [Manta Air, 2023], the inflation starts to work if the parachute has been deployed; this design is adopted for the RA3 UAS.

To model the airbag system for the RA3 UAS, a finite element (FE) model of airbag available in MADYMO version 2.1 [MADYMO, 2023] is implemented. This airbag FE model has been developed to simulate the complex behaviour of airbags during deployment and interaction with both vehicle and human body. The model primarily includes the airbag fabric, modelled as a flexible, foldable membrane mesh element with properties that reflect its real-world counterpart. [Happee et al., 2003].

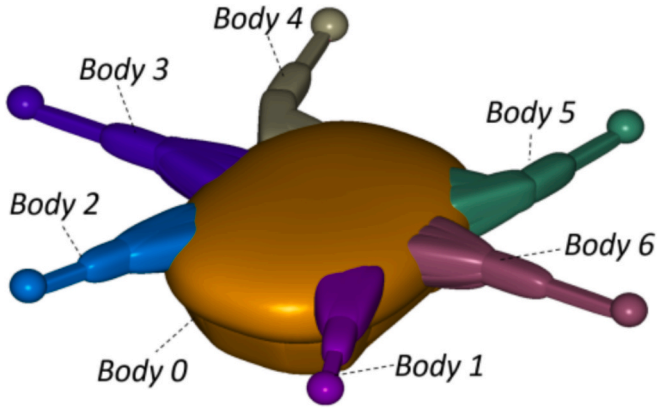

Fig. 2. Bodies in MBS model of RA3.

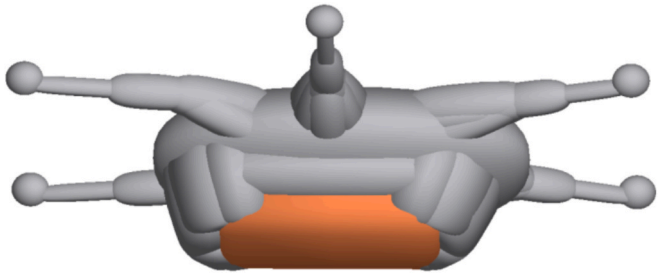

Fig. 3. Materials of RA3 UAS, body and arm made from carbon fibre (in grey); foam cargo box made from EPP foam (in orange). (For interpretation of the references to colour in this figure legend, the reader is referred to the web version of this article.)

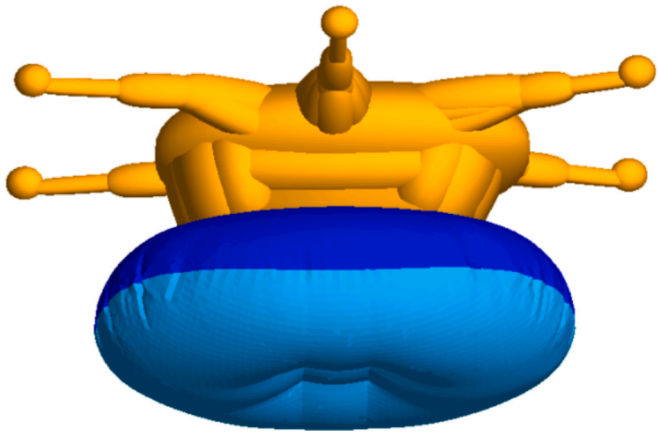

Fig. 4. Airbag FE model on bottom of the RA3 UAS MBS model.

In particular, [Happee et al., 2003] includes experimental validation of the FE airbag model in multiple scenarios—e.g., comparing simulated deployment kinematics to physical tests (folded and unfolded airbag inflations) [ADVANCE, 2003]. These studies underline that the modelling approach (membrane elements, contact definitions) can reliably capture real-world airbag performance. Building on this validated framework, we apply the same FE methodology here for the RA3 drone airbag, ensuring continuity with an experimentally benchmarked simulation technique.

The airbag FE model is anchored to the drone's MBS at a rigid patch near the inflator region. A fixed joint locks this patch to the bottom surface of drone, while the remainder of the airbag is free to deform. For airbag–drone interactions, a Multi-Body to Finite-Element (MB-FE) contact solver employs a penalty-based method (with user-defined friction) to prevent interpenetration. For airbag–human interactions, either FE-FE or MB-FE contact definitions (depending on the occupant model) similarly manage normal and tangential contact forces, referencing established force-penetration and damping curves.

The airbag's internal air is modeled using MADYMO's Unifor Pressure (UP) model [Happee et al., 2003; MADYMO, 2017b], which assumes an instantaneous and uniform distribution of pressure within the airbag. It also is assumed that the airbag is fully inflated prior to impact, and that there are no vent holes. Thanks to these assumptions, the model complexity and simulation runtime are manageable, and are expected to yield sufficient accuracy for our case, where collision velocity is relatively low (7–12 m/s).

The material properties typically assigned to the airbag fabric in the finite element model include elasticity, tensile strength, and tear resistance, which are crucial for accurately simulating how the fabric will unfold, inflate, and interact under pressure. For instance, upon inflation, the tension on fabric skin is determined by the material properties, with shear stiffness for woven fabric as shown in Fig. 5.

A two-step simulation procedure is adopted for the airbag equipped drone impacting on human. In Step 1, the Initial Metric Method (IMM) is used. The airbag starts folded at the drone's underside and is inflated until the desired internal pressure is reached and stabilized. The final stable mesh state and internal gas data are then stored. In Step 2, we import the stabilized mesh from Step 1 and reintroduce that same amount of air to the airbag during the first ~10 *ms* of the impact simulation. During this brief initial period, the airbag is temporarily "rigid", allowing the solver to match the previously stabilized pressure and shape without large deformations. Immediately after, the airbag is switched to a fully deformable state.

This two-step approach avoids repeatedly simulating the entire unfolding/inflation history for every impact scenario, thereby drastically reducing computational cost while maintaining physically accurate pressure and shape at the onset of the drone–human impact.

2.3. UAS impact on human

The MBS model of the human body adopted is a representative model for a mid-size (50th percentile) male human [Happee et al., 1998, 2000]. This human body MBS model (Fig. 6) is available in MADYMO (filename: h_occ50fc, version 5.2) and is used to simulation the impact of UAS on a 50th percentile male human.

Upon hitting a human body, the type of contacting UAS material and dynamic geometric effects are explicitly incorporated in the MBS model through three critical contact scenarios:

(i) Main fuselage-human head: Modeled as contact between a sphere and a flat surface with a Hertz contact model extended for inelastic impacts [Brake, 2012]. The effective contact radius and material-dependent modulus govern the nonlinear force–displacement relationship.

(ii) Motor arm-human head: Modeled as a sphere–sphere contact. Again, a Hertz contact model [Brake, 2012] is employed. During the contact, bending deformation on arms is also considered, which is determined by the torsional stiffness of the arm (Appendix A).

(iii) Cargo box-human head: the ellipsoid-foam contact model [Chou et al., 1994] is used. where the contact compliance curve is derived as the product of contact area and contact stress. The material properties (EPP foam at 70 kg/m^3) and associated load–unload curves are sourced from [Avalle et al., 2018].

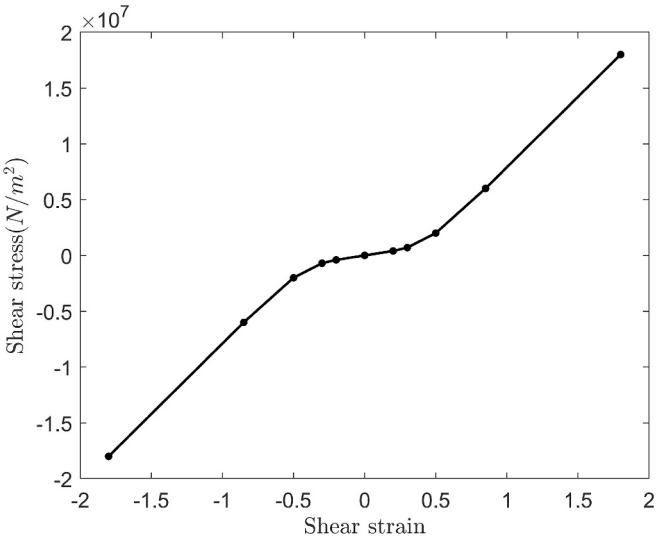

Fig. 5. Airbag fabric shear stiffness [Happee et al., 2003; MADYMO, 2020].

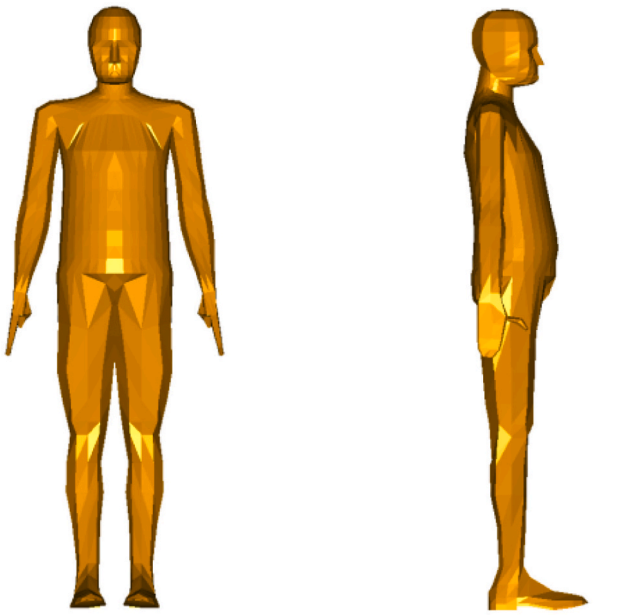

Fig. 6. 50th percentile human male body model.

In all cases, dynamic effects of varying materials and shapes are included through measured or literature-based compliance curves. These reflect how different materials (e.g., carbon fiber arms, fuselage shells, foam cargo boxes) behave upon impact on human body. Material properties and measured contact compliance curves for each contact scenario are presented in Appendix B.

The effect of UAS impact on human body is evaluated according to the following three injury criteria:

- Head Injury Criterion (HIC) for head injury;
- Neck Injury Criteria (N_{ij}) for neck injury;
- Viscous Criterion (VC) for thorax and abdomen injury.

All three injury criteria models are available within the dynamical simulation platform MADYMO. Head Injury Criterion (HIC) is an integrated value of head acceleration curve and represent the peak average power delivered to the head [Hutchinson et al., 1998]. HIC is widely adopted in car crash research, e.g. by the National Highway Traffic Safety Administration (NHTSA). Neck injury criteria N_{ij} are also widely adopted in car crash research. N_{ij} capture four types of neck loading N_{TF}, N_{TE}, N_{CF}, and N_{CE} [Eppinger et al., 1999]. The first subscript refers to Tension (i = T) and Compression (i=C) in axial direction. The second subscript refers to Flexion (j = F) and Extension (j = E) bending moments in the sagittal plane. Viscous Criterion (VC) is an injury criterion that has been developed for soft tissues [Lau and Viano, 1986], and therefore suitable for the evaluation of injury on thorax and abdomen.

2.4. Accumulation of multiple injury criteria into probability of fatality

The result of a dynamical simulation of a UAS collision with a human is quantified in terms of multiple injury levels: one for HIC, four for Nij, and two for VC. These seven injury levels typically depend on the horizontal offset Δ. So we need to convert, for each Δ, the seven assessed injury levels to a single value for $\mathbb{P}\{F|impact\}$. Such conversion is done in two steps.

During the first step, the HIC value is transformed to a HIC specific probability of fatality $\mathbb{P}\{F_{HIC}|impact\}$. Similarly, the four N_{ij} values are transformed to a N_{ij} specific probability of fatality $\mathbb{P}\{F_{NI}|impact\}$, and the two VC values for injuries on thorax and abdomen are transformed to a VC specific probability of fatality $\mathbb{P}\{F_{VC}|impact\}$. These first step transformations and corresponding curves are explained in Appendix C.

During the second step, the three probabilities of fatality $\mathbb{P}\{F_I|impact\}$, for $I \in \{HIC, NI, VC\}$, are probabilistically fused to the overall $\mathbb{P}\{F|impact\}$. For this fusion it is assumed that a human is not fatally injured if it is not fatally injured by Head injury, nor by Neck injury, and nor by VC injury. By assuming independence of these three events, we get:

$$\mathbb{P}\{F|impact\} = 1 - \prod_{I\in\{HIC,NI,VC\}} [1 - \mathbb{P}\{F_I|impact\}] \tag{3.1}$$

4. Dynamical simulation based method to assess the product $A_{impact}\bullet\mathbb{P}\{F|impact\}$

Jiang et al. (2024) develop a framework to assess the product $A_{impact}\bullet\mathbb{P}\{F|impact\}$ by conducting dynamical simulations. Subsection 4.1 explains the theory behind this framework. Subsection 4.2 develops a numerical method for this integration. Subsection 4.3 gives an overview of the resulting framework, and the simulation activities to be conducted for the RA3 UAS.

4.1. An integration model for the product $A_{impact}\bullet\mathbb{P}\{F|impact\}$

Jiang et al. (2024) have proven that the product $A_{impact}\bullet\mathbb{P}\{F|impact\}$ in (1.1) satisfies the following integral:

$$Q \triangleq A_{impact} \times \mathbb{P}\{F|impact\} = \int_{\mathbb{R}^2} \mathbb{P}\{F|\Delta\} d\Delta \tag{4.1}$$

where $\mathbb{P}\{F|\Delta\}$ is the conditional probability of fatality given horizontal offset Δ between the center of the UAS impact location relative to the location of an impacted human.

The derivation of Eq. (4.1) by [Jiang et al., 2024] works as follows. In [RCC, 2001], the term $\mathbb{P}\{F|impact\}$ is characterized as a summation over fatality probabilities in case a horizontal moving object impacts different body parts of a human, i.e.:

$$\mathbb{P}\{F|impact\} = \sum_B \left[\mathbb{P}\{F|\text{hit on body part } B\} \times \frac{\text{Area of body part } B}{\text{Area of human body}} \right] \tag{4.2}$$

In case of a UAS crashing from the air to the ground, the impact location of UAS can be at any horizontal offset Δ relative to the location of a human. To capture this falling UAS situation, the summation over body parts in Eq. (4.2) is replaced by an integration over all horizontal offsets Δ in the set $\{A_{impact}\}$, i.e.:

$$\mathbb{P}\{F|impact\} = \int_{\{A_{impact}\}} \mathbb{P}\{F|\Delta\} \frac{1}{A_{impact}} d\Delta \tag{4.3}$$

where $\mathbb{P}\{F|\Delta\}$ is the conditional probability of fatality given horizontal offset Δ.

Considering that $\mathbb{P}\{F|\Delta\} = 0$ for all $\Delta \notin \{A_{impact}\}$, Eq. (4.3) implies:

$$\mathbb{P}\{F|impact\} = \int_{\mathbb{R}^2} \mathbb{P}\{F|\Delta\} \frac{1}{A_{impact}} d\Delta \tag{4.4}$$

Multiplying both sides in Eq. (4.4) by A_{impact} yields Eq. (4.1).

4.2. Numerical evaluation of the integral in Eq. (4.1)

The next step is to numerically evaluate the integral in Eq. (4.1) to assess $Q \triangleq A_{impact} \times \mathbb{P}\{F|impact\}$. To accomplish this, we adopt a 2 dimensional grid for the relative positions between UAS and human body at moment of impact, and approximate (4.1) by a summation over the grid points Δ_i:

$$Q \triangleq A_{impact} \times \mathbb{P}\{F|impact\} \cong \sum_i \mathbb{P}\{F|\Delta_i\}|\Delta_i| \quad (4.5)$$

where $\mathbb{P}\{F|\Delta_i\}$ is the probability of fatality assessed through conducting dynamical simulations for the i-th grid point, and $|\Delta_i|$ is the 2D area size of the i-th grid point.

To assure that each dynamical simulation starts shortly before a possible hitting of human, the starting time τ of this dynamical situation is defined as the first moment that the drone center reaches a horizontal level that is R_{max} above top of human head, where R_{max} is the maximum range from drone center to drone edges. Fig. 7 shows the situation at this moment τ. Offset Δ is defined as the 2-dimensional horizontal offset between center of drone and center of human head at this moment τ (see Fig. 7b).

In addition to this offset Δ, human injury level also depends on the drone impact speed, course, descend angle, and attitude, as well as the human face direction φ_τ at this time moment τ. We assume that human face does not look up or down; hence human face direction may vary in horizontal direction only.

As is shown in Fig. 7b, by defining human face direction φ_τ relative to the course of the drone, there is no need for drone course as a model parameter. Hence the impact model parameters are: 2-dimensional offset Δ (defined at moment τ), horizontal face direction φ_τ, drone speed v_τ, descent angle ψ_τ, and 3-dimensional drone attitude θ_τ (pitch, roll, yaw).

During the MBS dynamical simulation, it is assumed that between time moment τ and the first hitting time (of human or ground), drone speed, descent angle, and attitude, as well as human face direction do not change.

4.3. Overview of the resulting framework

The dynamical simulation based TPR assessment methodology is visualized in Fig. 8. The three left hand boxes (i, ii, iii) in Fig. 8 represent the models developed in Section 3 for the RA3 UAS with airbag. Box iv defines the integration over the relevant grid values as has been explained in subsection 4.2. The central box v assesses injury levels for all grid values Δ. Box vi provides the transformations from subsection 4.3 of conditional injury levels given grid value Δ to conditional probability of fatality $\mathbb{P}\{F|\Delta\}$. Box vii uses the results from boxes iv, v and vi to produce the assessed TPR values.

5. Dynamical simulation results

Using the framework in Fig. 8, this section conducts dynamical simulations of RA3 UAS collision with a human for the three cases mentioned in the Introduction: Case A (RA3 with parachute and airbag), Case B (RA3 with parachute, no airbag), and Case C (RA3 without parachute/airbag). Subsection 5.1 provides Q results for cases A-C under zero wind, and face direction $\varphi = 0^\circ$. Subsection 5.2 extends these results to non-zero horizontal wind speeds. Subsection 5.3 compares the dynamical simulation results for cases B and C to those from parametric models in Table 3. Subsection 5.4 discusses the results obtained.

4.1. Dynamical simulation of **Q** under zero wind

For each of the three case A-C, dynamical simulations are conducted, under zero wind conditions, to assess $\mathbb{P}\{F|\Delta\}$ values for various offsets Δ for human impact, and human face direction $\varphi = 0^\circ$. As initial velocity conditions for the MBS/FE model based simulation collision of UAS with a human body, we adopt the velocities that have been assessed in Table 3 for cases B and C. It is also assumed that the inflated airbag does not influence the descent; hence descent velocity results for case B are assumed to also apply to case A.

The dynamical simulation assessed $\mathbb{P}\{F|\Delta\}$ values are shown in Table 4, Table 5 and Table 6 for cases A, B and C respectively, under descent angle $\psi = 90^\circ$ and face direction $\varphi = 0^\circ$. Note that due to face direction $\varphi = 0^\circ$, results are symmetrical for positive and negative cross offset $\Delta_\neg$ values, therefore results are only shown for positive cross offsets. The obtained $\mathbb{P}\{F|\Delta\}$ values are subsequently integrated over various offsets Δ values, using Eq. (4.5), to assess the corresponding Q value. These assessed Q values are specified in the captions of Tables 4-6 and collected in Table 7.

To gain a more complete understanding of the dynamical simulation results, we take a closer look at Tables 4-6. In all three tables, the white grid points are the same, i.e. in these grid points the RA3 does not touch human body. For the non-white grid points, Table 6 for case C shows the most simple picture: almost all grid points are red, which corresponds to 100 %, i.e. $\mathbb{P}\{F|\Delta\} = 1$. This means that for case C the terms A_{impact} and $\mathbb{P}\{F|impact\}$ are indeed almost independent. However, this simple picture does not apply to cases A and B. Table 5 for case B shows that many grid points that were red (100 %) for case C, have now orange or yellow colours, which reflect significant lower $\mathbb{P}\{F|\Delta\}$ values. In Table 4 for case A, for all grid points the red has changed to yellow, and a few to orange.

The of Q value results in Table 7 show that at zero wind, the equipped airbag and parachute (case A) reduces Q by a factor 8 relative to parachute only (case B), while the parachute alone reduces Q by another factor 3.3 relative to an unequipped RA3. Hence, the combination of parachute and airbag reduces ground TPR by a factor 25 x relative to an unequipped RA3 delivery UAS.

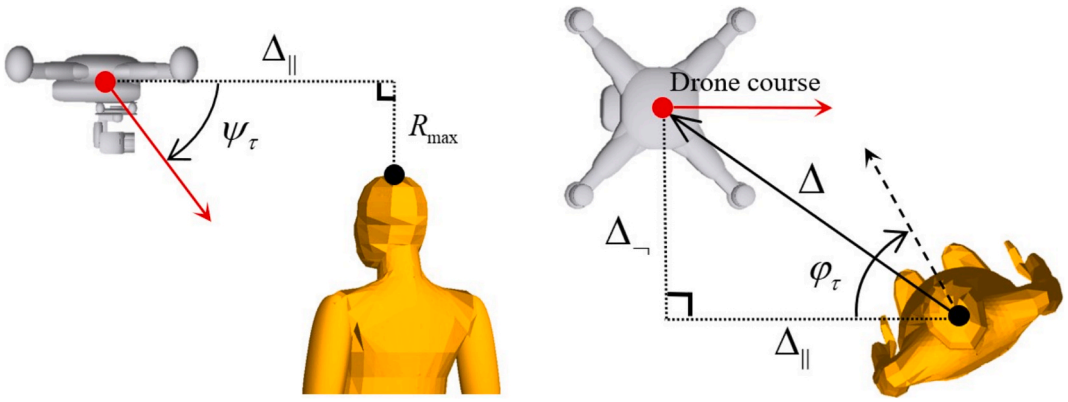

Fig. 7. Side view (a) and Top view (b) at moment τ, i.e. the moment that the drone descent with angle φ_τ and its centre reaches level R_{max} above top of human head with face direction φ_τ. R_{max} is the maximum range from drone mass centre to an edge of the drone. The top view (b) shows how the horizontal offset vector Δ between mass centres of drone and human head has components $\Delta\|$ and $\Delta_\neg$, that are parallel and perpendicular to drone course.

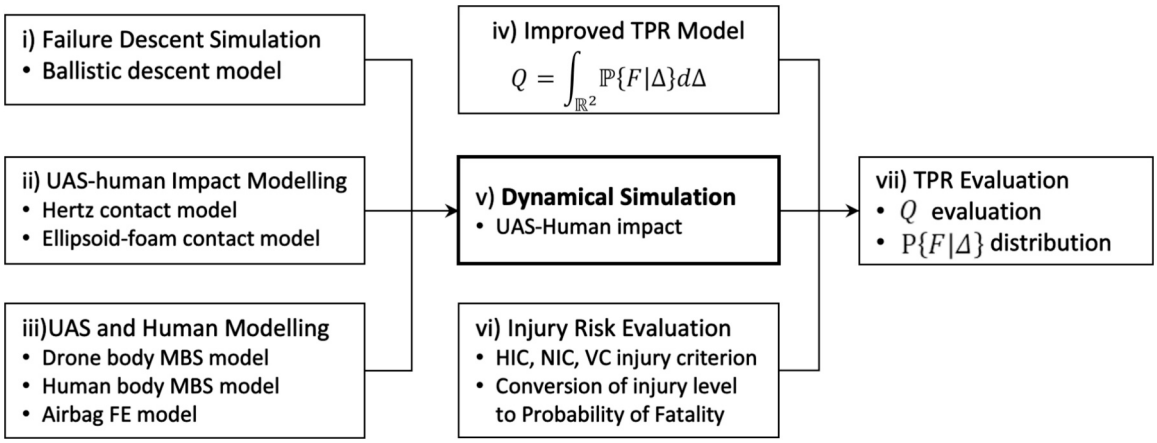

Fig. 8. Framework for dynamical simulation based evaluation of $Q \triangleq A_{impact} \times \mathbb{P}\{F|impact\}$.

Table 4
$\mathbb{P}\{F|\Delta\}$ (%), for case A, under zero wind. Impact velocity $|v| = 7.5m/s$, descent angle $\psi = 90^{\circ}$, face direction $\varphi = 0^{\circ}$. Red line shows the boundary outside which the UAS main body does not touch human body. The results are shown for positive cross offset $\Delta_{\neg}$ only, as the results are symmetrical for negative cross offset $\Delta_{\neg}$. Numerical integration, using Eq. (4.5), yields $Q = 0.031m^2$.

Along offset $\Delta_{\shortparallel}$ (m) \ Cross offset $\Delta_{\neg}$ (m)	0.00	0.05	0.10	0.15	0.20	0.25	0.30	0.35	0.40	0.45	0.50	0.55	0.60	0.65	0.70	0.75
0.70	0.0	0.0	0.0	0.0	0.0	0.0	0.0	0.0	0.0	0.0	0.0	0.0	0.0	0.0	0.0	0.0
0.65	0.0	0.0	0.0	0.0	0.0	2.7	3.1	2.8	0.0	0.0	0.0	0.0	0.0	0.0	0.0	0.0
0.60	0.0	0.0	0.0	0.0	0.0	3.0	4.2	3.7	0.0	0.0	0.0	0.0	0.0	0.0	0.0	0.0
0.55	0.0	0.0	0.0	0.0	0.0	3.5	4.5	3.8	0.0	0.0	0.0	0.0	0.0	0.0	0.0	0.0
0.50	0.0	0.0	0.0	0.0	0.0	3.9	4.6	3.9	0.0	0.0	0.0	0.0	0.0	0.0	0.0	0.0
0.45	3.7	3.7	3.3	2.7	2.7	4.8	5.1	0.6	0.0	0.0	0.0	0.0	0.0	0.0	0.0	0.0
0.40	4.6	4.7	4.1	3.6	3.9	5.9	5.7	3.8	0.0	0.0	0.0	0.0	0.0	0.0	0.0	0.0
0.35	13.4	16.5	8.2	4.5	4.3	5.4	6.8	3.8	0.0	0.0	0.0	0.0	0.0	0.0	0.0	0.0
0.30	20.7	10.8	20.9	55.8	5.1	5.5	21.7	3.6	0.0	0.0	0.0	0.0	0.0	0.0	0.0	0.0
0.25	7.4	6.7	9.2	24.2	7.1	3.5	4.6	0.0	0.0	0.0	0.0	0.0	0.0	0.0	0.0	0.0
0.20	6.4	5.7	5.8	21.8	16.9	3.2	4.4	0.0	0.0	0.0	0.0	0.0	0.0	0.0	0.0	0.0
0.15	6.9	5.9	4.9	5.0	4.8	3.1	2.8	0.0	0.0	0.0	0.0	0.0	0.0	0.0	0.0	0.0
0.10	6.0	5.6	4.8	4.0	3.5	3.0	3.0	6.4	4.6	4.3	3.6	3.2	3.0	2.9	0.0	0.0
0.05	4.8	4.2	4.0	3.7	3.5	3.1	5.2	24.7	6.7	5.8	5.0	4.6	3.8	3.8	0.0	00.
0.00	5.3	4.7	4.2	3.8	3.6	3.2	4.6	40.8	10.8	7.5	5.4	4.4	3.6	3.7	0.2	00.
-0.05	5.0	4.7	4.3	4.0	3.6	3.3	3.3	5.3	5.9	4.4	4.2	4.0	3.4	3.3	0.0	00.
-0.10	4.9	4.7	4.3	5.3	3.8	3.3	3.0	3.9	0.0	2.8	0.0	0.0	0.0	0.0	00.	00.
-0.15	4.7	4.5	5.1	6.2	9.0	3.2	2.9	0.0	0.0	0.0	0.0	0.0	0.0	0.0	0.0	0.0
-0.20	5.6	5.8	6.9	8.4	21.1	3.1	2.9	0.0	0.0	0.0	0.0	0.0	0.0	0.0	0.0	0.0
-0.25	30.5	28.4	15.6	45.4	4.8	3.4	3.5	0.0	0.0	0.0	0.0	0.0	0.0	0.0	0.0	0.0
-0.30	18.1	26.0	10.8	4.7	4.0	5.9	9.0	0.0	0.0	0.0	0.0	0.0	0.0	0.0	0.0	0.0
-0.35	4.5	4.5	4.3	4.7	5.5	18.5	4.3	0.0	0.0	0.0	0.0	0.0	0.0	0.0	0.0	0.0
-0.40	4.6	4.4	4.5	4.0	4.5	6.8	4.2	0.0	0.0	0.0	0.0	0.0	0.0	0.0	0.0	0.0
-0.45	0.0	0.0	0.0	0.0	3.9	4.4	4.2	3.0	0.0	0.0	0.0	0.0	0.0	0.0	0.0	0.0
-0.50	0.0	0.0	0.0	0.0	0.0	4.1	3.6	3.6	0.0	0.0	0.0	0.0	0.0	0.0	0.0	0.0
-0.55	0.0	0.0	0.0	0.0	0.0	3.5	4.0	3.5	0.0	0.0	0.0	0.0	0.0	0.0	0.0	0.0
-0.60	0.0	0.0	0.0	0.0	0.0	2.7	3.4	3.1	0.0	0.0	0.0	0.0	0.0	0.0	0.0	0.0
-0.65	0.0	0.0	0.0	0.0	0.0	0.0	0.0	0.0	0.0	0.0	0.0	0.0	0.0	0.0	0.0	0.0
-0.70	0.0	0.0	0.0	0.0	0.0	0.0	0.0	0.0	0.0	0.0	0.0	0.0	0.0	0.0	0.0	0.0

4.2. Dynamical simulation of **Q** under non-zero horizontal wind

For each of the three case A-C, dynamical simulations are conducted, under non-zero wind conditions, to assess $\mathbb{P}\{F|\Delta\}$ values for various offsets Δ for human impact, and human face direction $\varphi = 0^{\circ}$. As identified in subsection 5.1, the descend phase for case A is the same as it is for case B; which implies similarity in initial conditions of the dynamical simulation of the UAS impact with human. The key difference with subsection 5.1, is that due to non-zero wind the protecting effect of the airbag changes. This difference is depicted in Fig. 9a and b under 0 m/s and 10 m/s horizontal wind, for $\Delta = (0, 0)$.

Dynamical simulations, using the MBS or FE/MBS models, have been conducted to evaluate $\mathbb{P}\{F|\Delta\}$ for various offset values. For 10 m/s horizontal wind, these results are presented in Tables 8, 9 and 10 for cases A, B and C respectively. The obtained $\mathbb{P}\{F|\Delta\}$ values are subsequently integrated over various offsets Δ values, using Eq. (4.5); the resulting Q values are given in the captions of Tables 8, 9 and 10.

These MBS or FE/MBS model simulations have also been conducted for horizontal wind of 2, 4, 6 and 8 m/s. The resulting Q values for cases A, B and C are depicted in Fig. 10 as a function of horizontal wind speed. Hence, the left points of the curves in Fig. 10 are the Q assessments from Tables 4-6; the right points of these curves are the Q assessments from Tables 8-10.

Fig. 10 shows that for case C, horizontal wind has no effect on Q.

Table 5
$\mathbb{P}\{F|\Delta\}$ (%), for case B, under zero wind velocity, Impact velocity $|v| = 7.5m/s$, descent angle $\psi = 90^{\circ}$, face direction $\varphi = 0^{\circ}$. Red line shows the boundary outside which the UAS main body does not touch human body. The results are shown for positive cross offset $\Delta_{\neg}$ only, as the results are symmetrical for negative cross offset $\Delta_{\neg}$. Numerical integration, using Eq. (4.5), yields $Q = 0.256m^2$.

Along offset $\Delta_{\parallel}$ (m) \ Cross offset $\Delta_{\neg}$ (m)	0.00	0.05	0.10	0.15	0.20	0.25	0.30	0.35	0.40	0.45	0.50	0.55	0.60	0.65	0.70	0.75
0.70	0.0	0.0	0.0	0.0	0.0	0.0	0.0	0.0	0.0	0.0	0.0	0.0	0.0	0.0	0.0	0.0
0.65	0.0	0.0	0.0	0.0	0.0	2.7	3.1	2.8	0.0	0.0	0.0	0.0	0.0	0.0	0.0	0.0
0.60	0.0	0.0	0.0	0.0	0.0	3.0	4.2	3.7	0.0	0.0	0.0	0.0	0.0	0.0	0.0	0.0
0.55	0.0	0.0	0.0	0.0	0.0	3.5	4.5	3.8	0.0	0.0	0.0	0.0	0.0	0.0	0.0	0.0
0.50	0.0	0.0	0.0	0.0	0.0	3.9	4.6	3.9	0.0	0.0	0.0	0.0	0.0	0.0	0.0	0.0
0.45	0.0	0.0	0.0	0.0	2.8	4.9	5.3	0.7	0.0	0.0	0.0	0.0	0.0	0.0	0.0	0.0
0.40	5.2	5.2	5.1	0.0	4.1	6.3	6.0	3.8	0.0	0.0	0.0	0.0	0.0	0.0	0.0	0.0
0.35	32.5	37.8	38.8	5.1	7.6	10.7	7.7	3.9	0.0	0.0	0.0	0.0	0.0	0.0	0.0	0.0
0.30	78.5	94.1	91.8	43.1	5.5	85.9	35.7	3.8	0.0	0.0	0.0	0.0	0.0	0.0	0.0	0.0
0.25	75.3	97.0	83.7	93.1	78.3	54.4	70.8	0.0	0.0	0.0	0.0	0.0	0.0	0.0	0.0	0.0
0.20	73.4	97.8	98.9	100.0	93.4	14.3	32.0	0.0	0.0	0.0	0.0	0.0	0.0	0.0	0.0	0.0
0.15	19.5	54.9	100.0	91.6	66.1	5.2	4.5	0.0	0.0	0.0	0.0	0.0	0.0	0.0	0.0	0.0
0.10	43.3	39.8	27.2	52.5	81.5	6.8	63.3	19.6	4.8	4.3	3.7	3.2	3.0	2.9	0.0	0.0
0.05	58.3	52.8	42.2	34.7	94.3	9.6	90.4	73.8	7.8	6.2	5.2	4.6	3.8	3.8	0.0	0.0
0.00	63.7	58.0	46.1	37.6	94.3	10.7	89.1	88.9	15.1	8.9	5.8	4.4	3.6	3.7	0.2	0.0
-0.05	54.1	50.3	40.1	29.3	89.8	8.8	97.6	61.7	6.7	4.5	4.2	4.0	3.4	3.3	0.0	0.0
-0.10	37.3	34.4	46.7	61.7	52.0	8.7	36.1	3.7	0.0	2.9	0.0	0.0	0.0	0.0	0.0	0.0
-0.15	32.0	64.6	97.3	100.0	60.8	37.2	0.0	0.0	0.0	0.0	0.0	0.0	0.0	0.0	0.0	0.0
-0.20	60.2	87.7	80.0	100.0	91.0	6.7	2.9	0.0	0.0	0.0	0.0	0.0	0.0	0.0	0.0	0.0
-0.25	81.5	99.1	98.0	62.5	46.2	79.5	4.6	0.0	0.0	0.0	0.0	0.0	0.0	0.0	0.0	0.0
-0.30	57.0	87.4	89.7	15.4	16.5	81.3	9.9	0.0	0.0	0.0	0.0	0.0	0.0	0.0	0.0	0.0
-0.35	10.7	10.2	32.7	15.9	85.6	23.3	4.3	0.0	0.0	0.0	0.0	0.0	0.0	0.0	0.0	0.0
-0.40	10.1	8.9	5.2	3.9	4.7	6.9	4.3	0.0	0.0	0.0	0.0	0.0	0.0	0.0	0.0	0.0
-0.45	0.0	0.0	0.0	0.0	3.9	4.4	4.3	3.0	0.0	0.0	0.0	0.0	0.0	0.0	0.0	0.0
-0.50	0.0	0.0	0.0	0.0	0.0	4.1	3.7	3.7	0.0	0.0	0.0	0.0	0.0	0.0	0.0	0.0
-0.55	0.0	0.0	0.0	0.0	0.0	3.5	4.0	3.5	0.0	0.0	0.0	0.0	0.0	0.0	0.0	0.0
-0.60	0.0	0.0	0.0	0.0	0.0	2.7	3.4	3.1	0.0	0.0	0.0	0.0	0.0	0.0	0.0	0.0
-0.65	0.0	0.0	0.0	0.0	0.0	0.0	0.0	0.0	0.0	0.0	0.0	0.0	0.0	0.0	0.0	0.0
-0.70	0.0	0.0	0.0	0.0	0.0	0.0	0.0	0.0	0.0	0.0	0.0	0.0	0.0	0.0	0.0	0.0

Comparison of Table 10 and Table 6 shows that without airbag (case C) there hardly is an effect on $\mathbb{P}\{F|\Delta\}$. However, comparison of Tables 8 and 9 to Tables 4 and 5 shows that for cases A and B, the non-white area under horizontal wind of $10m/s$ is significantly larger than that under zero wind. Moreover, the area of red grid points for cases A and B is under $10m/s$ wind almost as large as it is for case C.

Fig. 10 shows that for cases A and B, the protecting effects of parachute and bottom airbag systematically decrease if the horizontal wind speed increases. Under $10m/s$ horizontal wind, the obtained Q values for case B are the same as for case C; i.e. $Q = 0.858m^2$ in Table 9 versus $Q = 0.859m^2$ in Table 10. This is only slightly better for case A: under $10m/s$ wind, the remaining reduction of Q by the parachute and airbag is less than a factor 1.3.

For case B, the explanation for the higher $Q = 0.858m^2$ under $10m/s$ wind, is that the horizontal wind of 10 m/s has two risk increasing effects: i) it increases the impact velocity ($12.5m/s$ compared to $7.5m/s$); and ii) it lowers the descent angle (37° compared to 90°). As can be seen in Table 9, the larger impact velocity results in higher probability of fatality for different impact locations, whereas the lower descent angle of 37° results in larger impact area for human head and now also includes human thorax and abdomen.

For case A, the explanation for the reduced effect of airbag under $10m/s$ wind can be seen from the results in Table 8. Due to the low descent angle of $\psi = 37^{\circ}$, the airbag only works for part of the offset locations. The $\mathbb{P}\{F|\Delta\}$ values for along offset values from $\Delta\| = 0.35m$ to $0.65m$ are significantly decreased. However, for the other offset values, the effect of airbag is negligible.

Now we know that due to the parachute effect, non-zero wind has significant impact on cases A and B, a follow-on question is to understand the influence of face direction. To answer this question, additional MBS simulations have been conducted for various face directions, under increasing horizontal wind velocities. The obtained $\mathbb{P}\{F|\Delta\}$ values have been integrated to Q; these results obtained for different face directions are shown in Fig. 11. The results in Fig. 11 show that the effect of human face direction φ is quite limited.

4.3. Comparison to using parametric model for $\boldsymbol{A_{impact}}$

We compare the dynamical simulation-based assessment results of $Q \triangleq A_{impact} \bullet \mathbb{P}\{F|impact\}$ for cases A, B and C to those obtained when adopting the parametric gliding model for A_{impact}, and the dynamical simulation results of $\mathbb{P}\{F|\Delta = (0, 0)\}$ for $\mathbb{P}\{F|impact\}$ in Section 2. Subsequently we compare and discuss the dynamical simulation results obtained for cases A-C.

The Q results obtained for cases A, B and C are collected in Tables 11, 12 and 13 respectively. For the parametric model results in these table, the gliding area model based results are presented.

The results in Table 11 show that for baseline case C, the dynamical modelling and simulation-based assessment results for $Q \triangleq A_{impact} \bullet \mathbb{P}\{F|impact\}$ are about a factor 3 x lower than the Gliding area based result. The main explanation for this difference can be identified by taking a look at the $\mathbb{P}\{F|\Delta\}$ results in Tables 6 and 10. These tables show that for case C, Q indeed is a product of the centre value $\mathbb{P}\{F|\Delta = (0, 0)\} = 1.0$ multiplied with the area size of the red grid points. The size of these red grid points is about a factor 3 x smaller than the sizes of the parametric gliding area models for case C.

The results in Table 12 show that for case B, the dynamical modelling and simulation based assessment results for $Q \triangleq A_{impact} \bullet \mathbb{P}\{F|impact\}$ are about an even larger factor (6.3 x and 7.5 x) lower than the Gliding area based results. The main explanation for this difference can be identified by taking a look at the $\mathbb{P}\{F|\Delta\}$ results in Tables 5 and 9. These tables show that for case B, Q is much more involved than a simple product of a

Table 6
$\mathbb{P}\{F|\Delta\}$ (%), for case C, as a function of cross offset $\Delta_\neg$ and along offset $\Delta\|$, under zero wind. Impact velocity $|v| = 40.6m/s$, descent angle $\psi = 90^\circ$, face direction $\varphi = 0^\circ$. Red line shows the boundary outside which the UAS main body does not touch human body. The results are shown for positive cross offset $\Delta_\neg$ only, as the results are symmetrical for negative cross offset $\Delta_\neg$. Numerical integration, using Eq. (4.5), yields $Q = 0.849m^2$.

Along offset $\Delta_\|$ (m) \ Cross offset $\Delta_\neg$ (m)	0.00	0.05	0.10	0.15	0.20	0.25	0.30	0.35	0.40	0.45	0.50	0.55	0.60	0.65	0.70	0.72
0.70	0.0	0.0	0.0	0.0	0.0	0.0	0.0	0.0	0.0	0.0	0.0	0.0	0.0	0.0	0.0	0.0
0.65	0.0	0.0	0.0	0.0	0.0	12.7	100	100	0.0	0.0	0.0	0.0	0.0	0.0	0.0	0.0
0.60	0.0	0.0	0.0	0.0	0.0	100	100	100	1.0	0.0	0.0	0.0	0.0	0.0	0.0	0.0
0.55	0.0	0.0	0.0	0.0	0.0	100	100	100	8.6	0.0	0.0	0.0	0.0	0.0	0.0	0.0
0.50	0.0	0.0	0.0	0.0	0.0	100	100	100	0.0	0.0	0.0	0.0	0.0	0.0	0.0	0.0
0.45	0.0	0.0	0.0	0.0	0.0	100	100	100	0.0	0.0	0.0	0.0	0.0	0.0	0.0	0.0
0.40	100	100	100	0.0	100	100	100	100	0.0	0.0	0.0	0.0	0.0	0.0	0.0	0.0
0.35	100	100	100	100	100	100	100	100	0.0	0.0	0.0	0.0	0.0	0.0	0.0	0.0
0.30	100	100	100	100	100	100	100	93.9	0.0	0.0	0.0	0.0	0.0	0.0	0.0	0.0
0.25	100	100	100	100	100	100	100	0.0	0.0	0.0	0.0	0.0	0.0	0.0	0.0	0.0
0.20	100	100	100	100	100	100	100	0.0	0.0	0.0	0.0	0.0	0.0	0.0	0.0	0.0
0.15	100	100	100	100	100	100	100	0.0	0.0	0.0	0.0	0.0	0.0	0.0	0.0	0.0
0.10	100	100	100	100	100	100	100	100	100	100	100	100	100	100	0.0	0.0
0.05	100	100	100	100	100	100	100	100	100	100	100	100	100	100	100	0.0
0.00	100	100	100	100	100	100	100	100	100	100	100	100	100	100	100	0.0
-0.05	100	100	100	100	100	100	100	100	100	100	100	100	100	100	85.9	0.0
-0.10	100	100	100	100	100	100	100	26.1	81.2	43.0	0.0	0.0	0.0	0.7	0.0	0.0
-0.15	100	100	100	100	100	100	0.0	0.0	0.0	0.0	0.0	0.0	0.0	0.0	0.0	0.0
-0.20	100	100	100	100	100	100	0.4	0.0	0.0	0.0	0.0	0.0	0.0	0.0	0.0	0.0
-0.25	100	100	100	100	100	100	100	0.0	0.0	0.0	0.0	0.0	0.0	0.0	0.0	0.0
-0.30	100	100	100	100	100	100	100	0.0	0.0	0.0	0.0	0.0	0.0	0.0	0.0	0.0
-0.35	100	100	100	100	100	100	100	0.0	0.0	0.0	0.0	0.0	0.0	0.0	0.0	0.0
-0.40	100	100	100	29.4	100	100	100	0.0	0.0	0.0	0.0	0.0	0.0	0.0	0.0	0.0
-0.45	0.0	0.0	0.0	0.0	100	100	100	100	0.0	0.0	0.0	0.0	0.0	0.0	0.0	0.0
-0.50	0.0	0.0	0.0	0.0	0.0	100	100	100	1.0	0.0	0.0	0.0	0.0	0.0	0.0	0.0
-0.55	0.0	0.0	0.0	0.0	0.0	100	100	100	3.0	0.0	0.0	0.0	0.0	0.0	0.0	0.0
-0.60	0.0	0.0	0.0	0.0	0.0	100	100	100	0.0	0.0	0.0	0.0	0.0	0.0	0.0	0.0
-0.65	0.0	0.0	0.0	0.0	0.0	0.0	1.3	0.0	0.0	0.0	0.0	0.0	0.0	0.0	0.0	0.0
-0.70	0.0	0.0	0.0	0.0	0.0	0.0	0.0	0.0	0.0	0.0	0.0	0.0	0.0	0.0	0.0	0.0

Table 7
Dynamical simulation-based assessment of Q values for cases A, B and C, under zero wind and face direction $\varphi = 0^\circ$.

Case	Q
A	0.031 m^2
B	0.256 m^2
C	0.849 m^2

centre value for $\mathbb{P}\{F|\Delta = (0,0)\}$ and an impact area size. The similarity between the two methods is that both assess that wind increase from $0m/s$ to $10m/s$ leads to a significant increase of the assessed Q values.

The results in Table 13 show that for case A, the dynamical modelling and simulation based assessment results for $Q \triangleq A_{impact} \bullet \mathbb{P}\{F|impact\}$ are about a factor (4.4 x and 9.5 x) lower than the Gliding area based results. The main explanation for this difference can be identified by taking a look at the $\mathbb{P}\{F|\Delta\}$ results in Tables 4 and 8. These tables show that for case A, Q is much more involved than a simple product of a centre value for $\mathbb{P}\{F|\Delta = (0,0)\}$ and an impact area size. The similarity between the two methods is that both assess that wind increase from $0m/s$ to $10m/s$ leads to a significant increase of the assessed Q values.

The above comparisons of cases A, B and C, and explanations of these differences, forms an initial validation of the dynamical models developed. For a further validation, common practice in safety risk literature is to also conduct a bias and uncertainty analysis. However, sensitivity and uncertainty analysis is still not yet found in ground TPR literature, and therefore falls out of scope of this research paper.

4.4. Discussion of results

In support of a discussion of results obtained, the Q results obtained through dynamical model-based simulation for cases A-C, under 0 m/s and 10 m/s side wind, are collected in Table 14.

Under $0m/s$ wind, the Q value assessed for case A is 8.5 x lower than for case B, and an extra factor 3.3 lower than case C. As has been

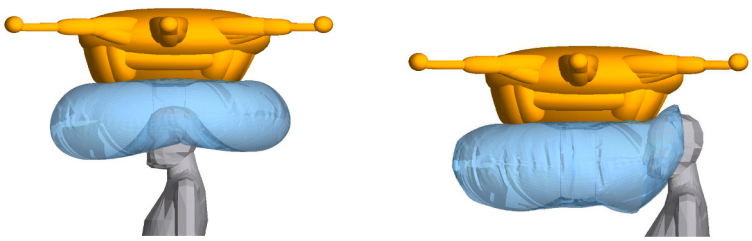

a. Impact under zero wind, $\psi = 90°$ **b**. Impact under 10 m/s horizontal wind, $\psi = 37°$

Fig. 9. Case A (with parachute and airbag) impact at zero offset, i.e. $\Delta = (0,0)$. The horizontal wind influences the impact decent angle ψ, with 10 m/s horizontal wind, the descent angle $\psi = 37^\circ$, which results in frontal impact on human.

Table 8
$\mathbb{P}\{F|\Delta\}$ (%), for case A, as a function of cross offset $\Delta_\neg$ and along offset $\Delta\|$, under $10m/s$ horizontal wind. Impact velocity $|v| = 12.5m/s$, descent angle $\psi = 37^\circ$, face direction $\varphi = 0^\circ$. Red line shows boundary outside which the UAS does not touch human body. The results are shown for positive cross offset $\Delta_\neg$ only, as the results are symmetrical for negative cross offset $\Delta_\neg$. Numerical integration, using Eq. (4.5), yields $Q = 0.677m^2$.

Along offset $\Delta_\|$ (m) \ Cross offset $\Delta_\neg$ (m)	0.00	0.05	0.1	0.15	0.2	0.25	0.3	0.35	0.4	0.45	0.5	0.55	0.6	0.65	0.7	0.75	0.8
0.75	0.0	0.0	0.0	0.0	0.0	0.0	0.0	0.0	0.0	0.0	0.0	0.0	0.0	0.0	0.0	0.0	0.0
0.7	0.0	0.0	0.0	0.0	0.0	0.0	3.3	2.7	0.0	0.0	0.0	0.0	0.0	0.0	0.0	0.0	0.0
0.65	0.0	0.0	0.0	0.0	0.0	4.5	14.2	4.6	0.0	0.0	0.0	0.0	0.0	0.0	0.0	0.0	0.0
0.6	0.0	0.0	0.0	0.0	0.0	0.0	1.1	1.5	0.0	0.0	0.0	0.0	0.0	0.0	0.0	0.0	0.0
0.55	0.0	0.0	0.0	0.0	0.0	0.0	0.0	1.1	0.0	0.0	0.0	0.0	0.0	0.0	0.0	0.0	0.0
0.5	0.0	0.0	0.0	0.0	0.0	0.0	0.0	1.2	0.0	0.0	0.0	0.0	0.0	0.0	0.0	0.0	0.0
0.45	0.0	0.0	0.0	0.0	0.0	0.0	0.0	1.1	0.0	0.0	0.0	0.0	0.0	0.0	0.0	0.0	0.0
0.4	0.0	1	1	1	0.0	0.0	0.0	1.8	0.0	0.0	0.0	0.0	0.0	0.0	0.0	0.0	0.0
0.35	1	4	21	19.2	1.4	0.0	0.0	1.6	0.0	0.0	0.0	0.0	0.0	0.0	0.0	0.0	0.0
0.3	13	9	80	50.1	21	0.6	0.0	1.2	0.0	0.0	0.0	0.0	0.0	0.0	0.0	0.0	0.0
0.25	100	100	97	96.4	58	1.3	0.0	0.2	0.0	0.0	0.0	0.0	0.0	0.0	0.0	0.0	0.0
0.2	100	100	62	100	10.4	5.6	13.3	0.0	0.0	0.0	0.0	0.0	0.0	0.0	0.0	0.0	0.0
0.15	91	81	100	100	88.2	16.3	100	99	9.9	2.3	4.7	4.2	3.8	3.4	0.0	0.0	0.0
0.1	100	100	100	100	100	48.8	100	100	49.5	38.8	5.8	4.5	4.4	4.0	2.9	0.0	0.0
0.05	100	100	100	100	100	1	100	100	89.7	51.8	11.9	6.1	4.4	4.1	3.7	0.0	0.0
0	100	100	100	100	100	46	100	100	97.8	66.3	16.4	6.1	4.8	4.2	1.1	0.0	0.0
-0.05	100	100	100	100	100	100	100	100	97.5	68.4	16.2	7.5	4.9	4.3	1.1	0.0	0.0
-0.1	100	100	100	100	100	100	100	100	89.3	46.1	11.9	5.0	4.2	1.4	0.8	0.0	0.0
-0.15	100	100	100	100	100	100	100	100	83.1	44.4	3.9	3.8	1.0	1.0	0.0	0.0	0.0
-0.2	100	100	100	100	100	100	12.4	0.0	0.0	0.0	0.0	0.0	0.0	0.0	0.0	0.0	0.0
-0.25	100	100	100	100	100	60.0	7.4	0.0	0.0	0.0	0.0	0.0	0.0	0.0	0.0	0.0	0.0
-0.3	100	100	100	100	88.0	85.5	60.7	0.0	0.0	0.0	0.0	0.0	0.0	0.0	0.0	0.0	0.0
-0.35	100	100	100	100	93.8	100	9.8	0.0	0.0	0.0	0.0	0.0	0.0	0.0	0.0	0.0	0.0
-0.4	100	100	100	100	100	30.2	5.2	3.0	0.0	0.0	0.0	0.0	0.0	0.0	0.0	0.0	0.0
-0.45	100	100	100	100	100	4.9	19.4	17.6	0.0	0.0	0.0	0.0	0.0	0.0	0.0	0.0	0.0
-0.5	100	100	100	100	76.7	20.8	95.3	100	2.9	0.0	0.0	0.0	0.0	0.0	0.0	0.0	0.0
-0.55	88.4	84.3	24.0	24.1	90.8	58.6	100	100	19.5	0.0	0.0	0.0	0.0	0.0	0.0	0.0	0.0
-0.6	2.7	16.0	18.0	11.0	49.6	88.6	100	100	40.5	0.0	0.0	0.0	0.0	0.0	0.0	0.0	0.0
-0.65	11.1	15.8	15.7	21.5	7.6	89.7	100	100	93.4	0.0	0.0	0.0	0.0	0.0	0.0	0.0	0.0
-0.7	14.4	15.3	13.0	18.8	18.3	100	100	100	27.6	0.0	0.0	0.0	0.0	0.0	0.0	0.0	0.0
-0.75	15.0	20.1	15.3	17.8	26.7	73.7	100	100	0.0	0.0	0.0	0.0	0.0	0.0	0.0	0.0	0.0
-0.8	12.6	13.0	8.0	3.2	8.1	12.4	97.0	59.8	0.0	0.0	0.0	0.0	0.0	0.0	0.0	0.0	0.0
-0.85	9.0	8.1	3.0	2.1	5.7	3.3	7.9	2.0	0.0	0.0	0.0	0.0	0.0	0.0	0.0	0.0	0.0
-0.9	6.9	5.4	2.4	0.0	5.4	1.0	1.1	0.8	0.0	0.0	0.0	0.0	0.0	0.0	0.0	0.0	0.0
-0.95	4.0	3.3	1.7	0.0	0.8	0.9	1.8	1.5	1.8	0.7	0.0	0.0	0.0	0.0	0.0	0.0	0.0
-1	3.6	2.4	1.1	0.0	0.0	1.1	3.6	3.8	3.9	1.1	0.0	0.0	0.0	0.0	0.0	0.0	0.0
-1.05	7.1	4.4	1.9	0.0	1.1	2.3	6.4	6.6	5.8	1.9	0.0	0.0	0.0	0.0	0.0	0.0	0.0
-1.1	7.6	5.0	1.1	0.0	1.0	3.4	7.7	9.5	9.7	3.4	0.8	0.0	0.0	0.0	0.0	0.0	0.0
-1.15	6.9	3.0	1.6	0.0	0.7	1.6	6.6	5.0	6.3	0.9	0.0	0.0	0.0	0.0	0.0	0.0	0.0
-1.2	10.4	4.4	2.5	0.8	0.0	0.9	2.7	3.8	3.2	1.4	0.0	0.0	0.0	0.0	0.0	0.0	0.0
-1.25	5.4	3.8	1.9	0.8	0.0	0.8	2.4	2.9	2.6	1.0	0.0	0.0	0.0	0.0	0.0	0.0	0.0
-1.3	1.5	1.3	0.9	1.1	0.0	0.8	2.5	3.6	2.1	0.9	0.0	0.0	0.0	0.0	0.0	0.0	0.0
-1.35	1.9	1.6	1.1	2.1	0.8	1.1	2.9	3.4	3.4	3.6	0.0	0.0	0.0	0.0	0.0	0.0	0.0
-1.4	2.7	1.6	0.0	0.0	2.5	4.6	6.6	8.4	6.8	3.2	0.0	0.0	0.0	0.0	0.0	0.0	0.0
-1.45	0.0	0.0	0.0	0.0	0.8	1.1	3.8	3.9	4.5	2.8	0.0	0.0	0.0	0.0	0.0	0.0	0.0
-1.5	0.0	0.0	0.0	0.7	3.7	1.9	4.3	4.2	5.4	12.8	0.0	0.0	0.0	0.0	0.0	0.0	0.0
-1.55	0.0	0.0	0.0	0.0	0.8	1.9	2.8	3.4	1.3	0.0	0.0	0.0	0.0	0.0	0.0	0.0	0.0
-1.6	0.0	0.0	0.0	0.0	0.0	0.0	0.0	0.0	0.0	0.0	0.0	0.0	0.0	0.0	0.0	0.0	0.0

explained in section 5.1, the latter factor is due to two RA3 design aspects: i) the deployed parachute reduces impact velocity; and ii) the bottom of the cargo box has a foam protection. The adding of a bottom airbag adds another factor 8.5 reduction.

Under $10m/s$ horizontal wind the Q value assessed for cases B and C are the same. The explanation is that although the parachute still significantly decreases impact velocity (from $40m/s$ to below $12.5m/s$), under $10m/s$ horizontal wind, the parachute also reduces the descent angle to as low as 37 degrees, resulting in larger impact area on human head, thorax and abdomen. Because an airbag placed on the bottom of the UAS does not really protect for this impact geometry, this also explains why for case A the Q value is reduced by 21 % only. This identified shortcoming of the bottom airbag considered, forms valuable feedback to the RA3 design process.

6. Dynamical modelling and simulation of airbag modifications

Feedback of the results obtained in section 5 to the UAS design immediately triggered ideas for improvements of the airbag design, followed by a second dynamical modelling and simulation cycle. Subsection 6.1 describes two proposals for airbag design change, and how these have been considered in the MBS/FE modelling. Subsection 6.2 conducts dynamical simulations with the MBS/FE models for these airbag changes and compares the results with those of section 5. Subsection 6.3 discusses the results obtained.

5.1. Airbag modifications

The feedback received from the assessment in section 5, has triggered two proposals for modifications in the airbag design. The first proposal is

Table 9

$\mathbb{P}\{F|\Delta\}$ (%), under horizontal wind velocity $10m/s$ for case B, as a function of cross offset $\Delta_\neg$ and along offset $\Delta\|$. Impact velocity $|v| = 12.5m/s$, descent angle $\psi = 37^\circ$, face direction $\varphi = 0^\circ$. Red line shows boundary outside which UAS does not touch human body. The results are shown for positive cross offset $\Delta_\neg$ only, as the results are symmetrical for negative cross offset $\Delta_\neg$. Numerical integration, using Eq. (4.5), yields $Q = 0.858m^2$.

Along offset $\Delta_\|$ (m) \ Cross offset $\Delta_\neg$ (m)	0.00	0.05	0.1	0.15	0.2	0.25	0.3	0.35	0.4	0.45	0.5	0.55	0.6	0.65	0.7	0.75	0.8
0.75	0.0	0.0	0.0	0.0	0.0	0.0	0.0	0.0	0.0	0.0	0.0	0.0	0.0	0.0	0.0	0.0	0.0
0.7	0.0	0.0	0.0	0.0	0.0	0.0	3.3	2.7	0.0	0.0	0.0	0.0	0.0	0.0	0.0	0.0	0.0
0.65	20.5	8.4	0	0	0	4.5	14.2	4.6	0.0	0.0	0.0	0.0	0.0	0.0	0.0	0.0	0.0
0.6	100	100	100	53.5	0	4.4	6.8	26.8	0.0	0.0	0.0	0.0	0.0	0.0	0.0	0.0	0.0
0.55	100	100	100	100	3.6	5.5	18.6	4.6	0.0	0.0	0.0	0.0	0.0	0.0	0.0	0.0	0.0
0.5	100	100	100	100	86.9	19.6	13.4	4.7	0.0	0.0	0.0	0.0	0.0	0.0	0.0	0.0	0.0
0.45	100	100	100	100	97.9	53.3	38.5	4.2	3.6	0.0	0.0	0.0	0.0	0.0	0.0	0.0	0.0
0.4	100	100	100	100	100	22.5	84.7	5.4	0.0	0.0	0.0	0.0	0.0	0.0	0.0	0.0	0.0
0.35	100	100	100	60.7	99.4	21.3	100	5.0	0.0	0.0	0.0	0.0	0.0	0.0	0.0	0.0	0.0
0.3	100	100	100	70.3	100	5.8	100	3.9	0.0	0.0	0.0	0.0	0.0	0.0	0.0	0.0	0.0
0.25	100	100	100	52.1	100	12.5	100	5.2	0.0	0.0	0.0	0.0	0.0	0.0	0.0	0.0	0.0
0.2	100	100	100	100	14.1	25.8	62.7	3.0	0.0	0.0	0.0	0.0	0.0	0.0	0.0	0.0	0.0
0.15	100	100	100	100	90.1	36.3	100	100	14.8	6.3	4.7	4.2	3.8	3.4	0.0	0.0	0.0
0.1	100	100	100	100	100	70.7	100	100	54.2	25.2	5.8	4.5	4.4	4.0	2.9	0.0	0.0
0.05	100	100	100	100	100	100	100	100	91.9	55.0	11.9	6.1	4.4	4.1	3.7	0.0	0.0
0	100	100	100	100	100	100	100	100	98.7	69.0	16.4	6.1	4.8	4.2	1.1	0.0	0.0
-0.05	100	100	100	100	100	100	100	100	98.5	70.7	16.2	7.5	4.9	4.3	1.1	0.0	0.0
-0.1	100	100	100	100	100	100	100	100	89.3	46.1	11.9	5.0	4.2	1.4	0.8	0.0	0.0
-0.15	100	100	100	100	100	100	100	100	83.1	44.4	3.9	3.8	1.0	1.0	0.0	0.0	0.0
-0.2	100	100	100	100	100	100	12.4	0.0	0.0	0.0	0.0	0.0	0.0	0.0	0.0	0.0	0.0
-0.25	100	100	100	100	100	60.0	7.4	0.0	0.0	0.0	0.0	0.0	0.0	0.0	0.0	0.0	0.0
-0.3	100	100	100	100	88.0	85.5	60.7	0.0	0.0	0.0	0.0	0.0	0.0	0.0	0.0	0.0	0.0
-0.35	100	100	100	100	93.8	100	9.8	0.0	0.0	0.0	0.0	0.0	0.0	0.0	0.0	0.0	0.0
-0.4	100	100	100	100	100	30.2	5.2	3.0	0.0	0.0	0.0	0.0	0.0	0.0	0.0	0.0	0.0
-0.45	100	100	100	100	100	4.9	19.4	17.6	0.0	0.0	0.0	0.0	0.0	0.0	0.0	0.0	0.0
-0.5	100	100	100	100	76.7	20.8	95.3	100	2.9	0.0	0.0	0.0	0.0	0.0	0.0	0.0	0.0
-0.55	88.4	84.3	24.0	24.1	90.8	58.6	100	100	19.5	0.0	0.0	0.0	0.0	0.0	0.0	0.0	0.0
-0.6	2.7	16.0	18.0	11.0	49.6	88.6	100	100	40.5	0.0	0.0	0.0	0.0	0.0	0.0	0.0	0.0
-0.65	11.1	15.8	15.7	21.5	7.6	89.7	100	100	93.4	0.0	0.0	0.0	0.0	0.0	0.0	0.0	0.0
-0.7	14.4	15.3	13.0	18.8	18.3	100	100	100	27.6	0.0	0.0	0.0	0.0	0.0	0.0	0.0	0.0
-0.75	15.0	20.1	15.3	17.8	26.7	73.7	100	100	0.0	0.0	0.0	0.0	0.0	0.0	0.0	0.0	0.0
-0.8	12.6	13.0	8.0	3.2	8.1	12.4	97.0	59.8	0.0	0.0	0.0	0.0	0.0	0.0	0.0	0.0	0.0
-0.85	9.0	8.1	3.0	2.1	5.7	3.3	7.9	2.0	0.0	0.0	0.0	0.0	0.0	0.0	0.0	0.0	0.0
-0.9	6.9	5.4	2.4	0.0	5.4	1.0	1.1	0.8	0.0	0.0	0.0	0.0	0.0	0.0	0.0	0.0	0.0
-0.95	4.0	3.3	1.7	0.0	0.8	0.9	1.8	1.5	1.8	0.7	0.0	0.0	0.0	0.0	0.0	0.0	0.0
-1	3.6	2.4	1.1	0.0	0.0	1.1	3.6	3.8	3.9	1.1	0.0	0.0	0.0	0.0	0.0	0.0	0.0
-1.05	7.1	4.4	1.9	0.0	1.1	2.3	6.4	6.6	5.8	1.9	0.0	0.0	0.0	0.0	0.0	0.0	0.0
-1.1	7.6	5.0	1.1	0.0	1.0	3.4	7.7	9.5	9.7	3.4	0.8	0.0	0.0	0.0	0.0	0.0	0.0
-1.15	6.9	3.0	1.6	0.0	0.7	1.6	6.6	5.0	6.3	0.9	0.0	0.0	0.0	0.0	0.0	0.0	0.0
-1.2	10.4	4.4	2.5	0.8	0.0	0.9	2.7	3.8	3.2	1.4	0.0	0.0	0.0	0.0	0.0	0.0	0.0
-1.25	5.4	3.8	1.9	0.8	0.0	0.8	2.4	2.9	2.6	1.0	0.0	0.0	0.0	0.0	0.0	0.0	0.0
-1.3	1.5	1.3	0.9	1.1	0.0	0.8	2.5	3.6	2.1	0.9	0.0	0.0	0.0	0.0	0.0	0.0	0.0
-1.35	1.9	1.6	1.1	2.1	0.8	1.1	2.9	3.4	3.4	3.6	0.0	0.0	0.0	0.0	0.0	0.0	0.0
-1.4	2.7	1.6	0.0	0.0	2.5	4.6	6.6	8.4	6.8	3.2	0.0	0.0	0.0	0.0	0.0	0.0	0.0
-1.45	0.0	0.0	0.0	0.0	0.8	1.1	3.8	3.9	4.5	2.8	0.0	0.0	0.0	0.0	0.0	0.0	0.0
-1.5	0.0	0.0	0.0	0.7	3.7	1.9	4.3	4.2	5.4	12.8	0.0	0.0	0.0	0.0	0.0	0.0	0.0
-1.55	0.0	0.0	0.0	0.0	0.8	1.9	2.8	3.4	1.3	0.0	0.0	0.0	0.0	0.0	0.0	0.0	0.0
-1.6	0.0	0.0	0.0	0.0	0.0	0.0	0.0	0.0	0.0	0.0	0.0	0.0	0.0	0.0	0.0	0.0	0.0

to increase the pressure of the bottom airbag from 1 atm (atmospheric pressure), i.e. equal to environment, to 1.1 atm. This design modification is referred to as A1. The second proposal is to equip the RA3 with a second deployable airbag at the front of RA3; both airbags are assumed to have the higher pressure of 1.1 atm. This design modification is referred to as A2.

The dynamic modelling of modification A1 is accomplished by changing the atmospheric pressure setting parameter in the FE airbag model. Design modification A2 involves the inclusion of a front airbag in the FE/MBS model. To accomplish this, the front airbag is assumed to be of similar design as the bottom airbag; this makes it possible to use the same FE model for the front airbag, with the only need to adapt the airbag size. Furthermore, we assume that under influence of wind, the front airbag captures more wind, as a result of which the front of the RA3 UAS will reach human body first. For these two modifications, the initial hitting of the RA3 with airbag(s) under $10m/s$ horizontal wind is depicted in Fig. 12a and b for cases A1 and A2 respectively.

5.2. Dynamical simulation of airbag modifications

For cases A1 and A2, dynamical simulations have been conducted to assess $\mathbb{P}\{F|\Delta\}$ values for horizontal wind ranging from 0 m/s to $10m/s$; this is shown in Tables 15 and 16.

The obtained $\mathbb{P}\{F|\Delta\}$ values are integrated to Q results; these results are shown in Fig. 13 for cases A1 and A2, together with the curves obtained in section 5 for cases A and B. The curve for case A1 shows that the increased risk can partly be mitigated by using a bottom airbag with 1.1 atmosphere pressure. The curve for case A2 shows that this risk is further mitigated by adding an additional front airbag at 1.1 atmosphere pressure.

Table 10
$\mathbb{P}\{F|\Delta\}$ (%), under $10m/s$ horizontal wind for case C, as a function of cross offset $\Delta_\neg$ and along offset $\Delta\|$. Impact velocity $|v| = 40.4m/s$, descent angle $\psi = 84.7^\circ$, face direction $\varphi = 0^\circ$. Red line shows boundary outside which UAS does not touch human body. The results are shown for positive cross offset $\Delta_\neg$ only, as the results are symmetrical for negative cross offset $\Delta_\neg$. Numerical integration, using Eq. (4.5), yields $Q = 0.859m^2$.

Along offset $\Delta_\|$ (m) \ Cross offset $\Delta_\neg$ (m)	0.00	0.05	0.10	0.15	0.20	0.25	0.30	0.35	0.40	0.45	0.50	0.55	0.60	0.65	0.70	0.75
0.70	0.0	0.0	0.0	0.0	0.0	0.0	0.0	0.0	0.0	0.0	0.0	0.0	0.0	0.0	0.0	0.0
0.65	0.0	0.0	0.0	0.0	0.0	10.7	100	98.3	0.0	0.0	0.0	0.0	0.0	0.0	0.0	0.0
0.60	0.0	0.0	0.0	0.0	0.0	100	100	100	3.3	0.0	0.0	0.0	0.0	0.0	0.0	0.0
0.55	0.0	0.0	0.0	0.0	0.0	100	100	100	6.9	0.0	0.0	0.0	0.0	0.0	0.0	0.0
0.50	0.0	0.0	0.0	0.0	0.0	100	100	100	3.5	0.0	0.0	0.0	0.0	0.0	0.0	0.0
0.45	0.0	0.0	0.0	0.0	2.8	100	100	100	0.0	0.0	0.0	0.0	0.0	0.0	0.0	0.0
0.40	100	100	100	0.0	100	100	100	100	0.0	0.0	0.0	0.0	0.0	0.0	0.0	0.0
0.35	100	100	100	100	100	100	100	100	0.0	0.0	0.0	0.0	0.0	0.0	0.0	0.0
0.30	100	100	100	100	100	100	100	98.9	0.0	0.0	0.0	0.0	0.0	0.0	0.0	0.0
0.25	100	100	100	100	100	100	100	3.4	0.0	0.0	0.0	0.0	0.0	0.0	0.0	0.0
0.20	100	100	100	100	100	100	100	0.0	0.0	0.0	0.0	0.0	0.0	0.0	0.0	0.0
0.15	100	100	100	100	100	100	100	0.0	0.0	0.0	0.0	0.0	0.0	0.0	0.0	0.0
0.10	100	100	100	100	100	100	100	100	100	100	100	100	100	100	0.0	0.0
0.05	100	100	100	100	100	100	100	100	100	100	100	100	100	100	100	0.0
0.00	100	100	100	100	100	100	100	100	100	100	100	100	100	100	100	0.0
-0.05	100	100	100	100	100	100	100	100	100	100	100	100	100	100	89.7	0.0
-0.10	100	100	100	100	100	100	100	100	100	100	9.9	8.1	3.5	3.8	0.0	0.0
-0.15	100	100	100	100	100	100	0.0	0.0	0.0	0.0	0.0	0.0	0.0	0.0	0.0	0.0
-0.20	100	100	100	100	100	100	3.0	0.0	0.0	0.0	0.0	0.0	0.0	0.0	0.0	0.0
-0.25	100	100	100	100	100	100	100	0.0	0.0	0.0	0.0	0.0	0.0	0.0	0.0	0.0
-0.30	100	100	100	100	100	100	100	0.0	0.0	0.0	0.0	0.0	0.0	0.0	0.0	0.0
-0.35	100	100	100	100	100	100	100	0.0	0.0	0.0	0.0	0.0	0.0	0.0	0.0	0.0
-0.40	100	100	100	53.8	100	100	100	0.0	0.0	0.0	0.0	0.0	0.0	0.0	0.0	0.0
-0.45	0.0	0.0	0.0	0.0	100	100	100	100	0.0	0.0	0.0	0.0	0.0	0.0	0.0	0.0
-0.50	0.0	0.0	0.0	0.0	0.0	100	100	100	4.1	0.0	0.0	0.0	0.0	0.0	0.0	0.0
-0.55	0.0	0.0	0.0	0.0	0.0	100	100	100	13.1	0.0	0.0	0.0	0.0	0.0	0.0	0.0
-0.60	0.0	0.0	0.0	0.0	0.0	100	100	100	0.0	0.0	0.0	0.0	0.0	0.0	0.0	0.0
-0.65	0.0	0.0	0.0	0.0	0.0	0.0	4.4	5.0	0.0	0.0	0.0	0.0	0.0	0.0	0.0	0.0
-0.70	0.0	0.0	0.0	0.0	0.0	0.0	0.0	0.0	0.0	0.0	0.0	0.0	0.0	0.0	0.0	0.0

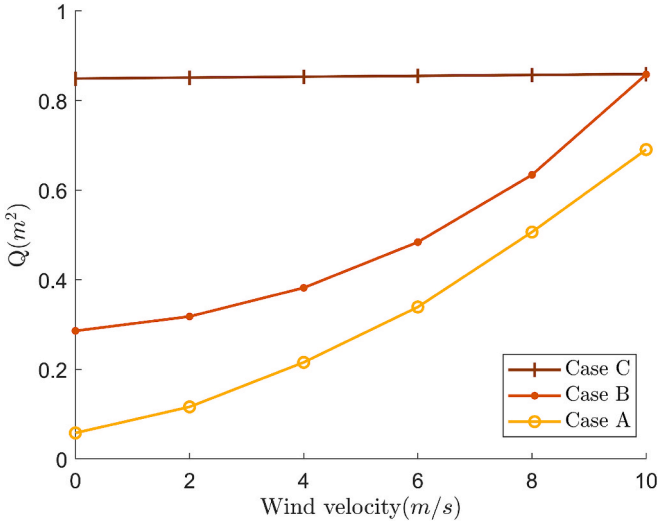

Fig. 10. Q for case A (parachute and airbag), case B (parachute, no airbag), and case C (no parachute, no airbag) as a function of horizontal wind velocity, for face direction $\varphi = 0^\circ$.

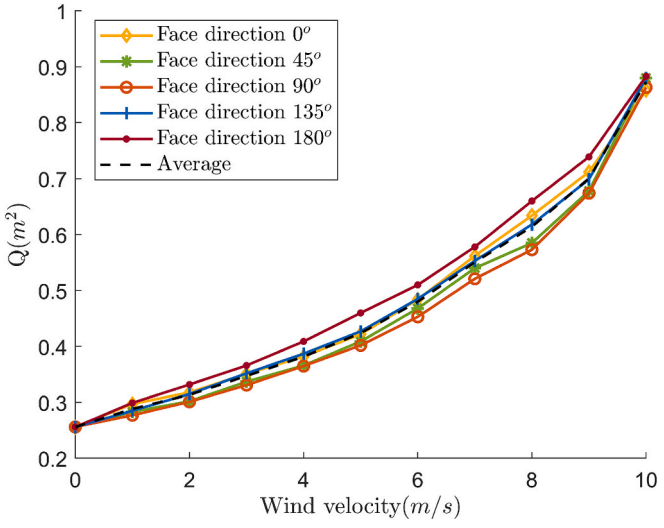

Fig. 11. Q for case B, as a function of horizontal wind velocity, for face direction $\varphi \in \{0^\circ, 45^\circ, 90^\circ, 135^\circ, 180^\circ\}$, where $\varphi = 0^\circ$ stands for face in the wind.

Even for case A2, the risk still increases to a relative high level if wind velocity increases. The higher wind velocity leads to higher impact velocity and lower descent angle. The increased impact velocity results in higher risk for impact on drone arms that are not covered by airbag. The lower descent angle leads to non-vertical and non-central impacts on airbag that results in higher risk, as the airbag is not designed for such types of impact. This can be seen from the $\mathbb{P}\{F|\Delta\}$ values in Table 16 for case A2 and 10 m/s horizontal wind velocity. The high-risk areas are for those drone arm impacts and non-central impacts on bottom and side airbags.

5.3. Discussion of results obtained for the airbag modifications

Table 17 collects the assessed Q values for cases A1, and A2 under $0m/s$, $4m/s$ and $10m/s$ wind, together with the corresponding values

Table 11
Comparison of Q assessment for case C: Dynamical simulation versus Gliding area model.

	$\mathbb{P}\{F\|\Delta=(0,0)\}\times$ Gliding area	Q from Dynamical simulation	Reduction Factor
0 m/s wind	$1.0\times 2.55\ m^2=2.55\ m^2$	$0.849\ m^2$	3 x
10 m/s wind	$1.0\times 2.81\ m^2=2.81\ m^2$	$0.859\ m^2$	3.3 x

Table 12
Comparison of Q assessment for case B: Dynamical simulation versus Gliding area model.

	$\mathbb{P}\{F\|\Delta=(0,0)\}\times$ Gliding area	Q from Dynamical simulation	Reduction Factor
0 m/s wind	$0.64\times 2.55\ m^2=1.62\ m^2$	$0.256\ m^2$	6.3 x
10 m/s wind	$1.0\times 6.45\ m^2=6.45\ m^2$	$0.858\ m^2$	7.5 x

Table 13
Comparison of Q assessment for case A: Dynamical simulation versus Gliding area model.

	$\mathbb{P}\{F\|\Delta=(0,0)\}\times$ Gliding area	Q from Dynamical simulation	Reduction Factor
0 m/s wind	$0.053\times 2.55\ m^2=0.13\ m^2$	$0.031\ m^2$	4.4 x
10 m/s wind	$1.00\times 6.45\ m^2=6.45\ m^2$	$0.68\ m^2$	9.5 x

Table 14
Comparison of dynamical simulation based Q assessment for cases A, B, C.

Q	Case A	Case B	Case C
0 m/s wind	$0.031\ m^2$	$0.256\ m^2$	$0.849\ m^2$
10 m/s wind	$0.677\ m^2$	$0.858\ m^2$	$0.859\ m^2$

assessed for cases A, B and C. Under $0m/s$ wind, modifications A1 and A2 only slightly improve the protection provided by the original airbag design (case A); i.e. a factor 34 x over case C. Under 4 m/s wind, modifications A1 and A2 still are very effective in reducing the assessed Q value; i.e. a factor 17 x for A2 relative to case C. Above $4m/s$ wind the risk reducing effect steadily decreases, to a factor 1.9 under $10m/s$ wind for A2 relative to case C.

These results obtained for the airbag design modifications show that the developed dynamical modelling and simulation approach can provide effective safety feedback to the design process of a novel UAS.

7. Conclusion

As has been explained in section 1, parachute and airbag influence ground TPR in a linear way through the product $A_{impact}\bullet\mathbb{P}\{F|impact\}$, with A_{impact} the size of the "crash impact area" on the ground, and $\mathbb{P}\{F|impact\}$ the probability of Fatality (F) for a person in the "crash impact area". Section 1 also formulated the research objective: "to apply both the existing dynamical modelling and simulation method and a novel method of [Jiang et al., 2024] to the assessment of the product $A_{impact}\bullet\mathbb{P}\{F|impact\}$ for a small parcel delivery UAS that is equipped with deployable parachute and airbag, and to feedback the findings to the UAS design". This research objective has been realized as follows.

Section 2 has specified the RA3 UAS of 15 kg that is under design, and has applied existing parametric models from literature for the assessment of both A_{impact} and $\mathbb{P}\{F|impact\}$. These parametric models do not apply to a UAS that is equipped with an airbag. Moreover, according to the parametric model results obtained, equipping an RA3 with a deployable parachute does not even help to reduce the product $A_{impact}\bullet\mathbb{P}\{F|impact\}$ for the RA3 UAS.

Section 3 has developed four types of dynamical models to simulate the dynamical interaction between RA3, its bottom airbag and human body in case of a hit. These models are: i) an MBS model for the RA3 UAS; ii) an FE model for a deployed bottom airbag; iii) a model for the contact with human body parts; and iv) a model to transform injury levels to $\mathbb{P}\{F|impact\}$.

Section 4 explained the novel method of [Jiang et al., 2024] in using the models developed in Section 3 for a simulation-based assessment of the product $A_{impact}\bullet\mathbb{P}\{F|impact\}$ instead of $\mathbb{P}\{F|impact\}$ alone, and to combine this with a parametric model for A_{impact}.

Section 5 has applied the models and method from sections 3 and 4 to three cases of RA3 crashes to the ground. Case A: RA3 with parachute and airbag; case B: RA3 with parachute only; and Case C: RA3 without parachute/airbag. For the results obtained with the novel method of [Jiang et al., 2024] two comparisons have been made: i) Comparison for cases A, B and C, of the results from the novel method versus results using a parametric model for A_{impact}; and ii) Comparison of the differences between the results from the novel method for cases A, B and C. Comparison i) has shown that the results from the novel method yields $A_{impact}\bullet\mathbb{P}\{F|impact\}$ values that are a factor 3x-9x lower than using a parametric model for A_{impact}. From a ground TPR assessment perspective this means that a UAS can be certified to fly over a 3x higher population density. Comparison ii) show that the assessed values for the product $A_{impact}\bullet\mathbb{P}\{F|impact\}$ differ significantly for three cases (A, B, C). Under zero wind case A yields a factor 8.25 x in risk reduction relative to case B, and a factor 27 x relative to case C. It was also found that both these factors decrease under increasing wind conditions.

Section 6 uses the feedback received from the dynamical simulation results in section 5 to two proposals for the modification of the original airbag design. Modification A1 is to increase the pressure of the bottom

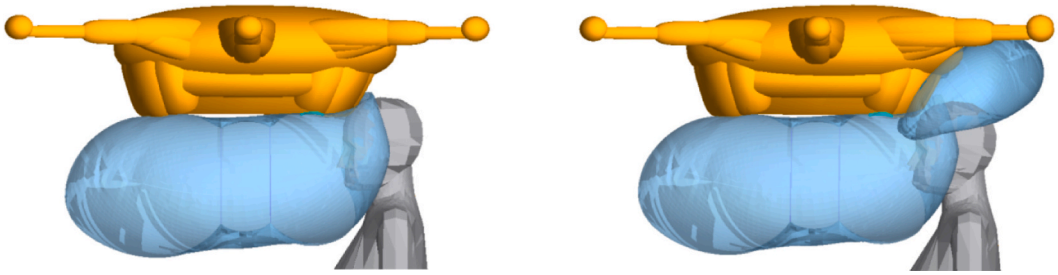

a. Pressure of bottom airbag is 1.1 atm. **b.** Adding a front airbag, both at 1.1 atm.

Fig. 12. Expected effect airbag design modifications A1 and A2 for an impact at zero offset, i.e. $\Delta=(0,0)$ with 10 m/s horizontal wind.

Table 15
$\mathbb{P}\{F|\Delta\}$ (%), for case A1 (1.1 atmosphere pressure in bottom airbag), as a function of cross offset $\Delta_{\neg}$ and along offset $\Delta_{\|}$, under $10m/s$ horizontal wind. Impact velocity $|v| = 12.5m/s$, descent angle $\psi = 37^{\circ}$, face direction $\varphi = 0^{\circ}$. Red line shows the boundary outside which the UAS does not touch human body. The results are shown for positive cross offset $\Delta_{\neg}$ only, as the results are symmetrical for negative cross offset $\Delta_{\neg}$. Numerical integration, using Eq. (4.5), yields $Q = 0.638m^2$.

Along offset $\Delta_{\|}$ (m) \ Cross offset $\Delta_{\neg}$ (m)	0.00	0.05	0.10	0.15	0.20	0.25	0.30	0.35	0.40	0.45	0.50	0.55	0.60	0.65	0.70	0.75	0.80
0.75	0.0	0.0	0.0	0.0	0.0	0.0	0.0	0.0	0.0	0.0	0.0	0.0	0.0	0.0	0.0	0.0	0.0
0.70	0.0	0.0	0.0	0.0	0.0	0.0	3.3	2.7	0.0	0.0	0.0	0.0	0.0	0.0	0.0	0.0	0.0
0.65	7.8	7.3	6.2	5.2	4.3	3.8	3.6	0.0	0.0	0.0	0.0	0.0	0.0	0.0	0.0	0.0	0.0
0.60	6.5	6.4	6.4	5.3	4.1	3.6	3.4	2.7	0.0	0.0	0.0	0.0	0.0	0.0	0.0	0.0	0.0
0.55	5.4	5.4	5.6	4.7	3.9	3.3	3.1	2.7	0.0	0.0	0.0	0.0	0.0	0.0	0.0	0.0	0.0
0.50	4.4	5.9	5.0	4.6	4.0	3.0	2.9	2.8	0.0	0.0	0.0	0.0	0.0	0.0	0.0	0.0	0.0
0.45	4.4	4.4	4.3	4.2	3.8	3.2	3.0	2.8	0.0	0.0	0.0	0.0	0.0	0.0	0.0	0.0	0.0
0.40	4.7	4.7	4.6	4.3	3.8	3.3	3.0	2.8	0.0	0.0	0.0	0.0	0.0	0.0	0.0	0.0	0.0
0.35	5.2	5.0	4.9	4.5	4.0	3.5	3.1	2.8	0.0	0.0	0.0	0.0	0.0	0.0	0.0	0.0	0.0
0.30	6.8	7.0	6.9	5.2	4.1	3.6	3.1	2.8	0.0	0.0	0.0	0.0	0.0	0.0	0.0	0.0	0.0
0.25	10.1	13.0	9.2	13.9	4.0	3.6	3.1	2.8	0.0	0.0	0.0	0.0	0.0	0.0	0.0	0.0	0.0
0.20	11.6	16.8	83.1	71.8	4.8	3.5	3.3	5.7	0.0	0.0	0.0	0.0	0.0	0.0	0.0	0.0	0.0
0.15	100	100	100	100	91.7	3.4	19.8	89.3	9.9	2.3	4.7	4.2	3.8	3.4	0.0	0.0	0.0
0.10	100	100	100	100	100	4.0	100	100	49.5	38.8	5.8	4.5	4.4	4.0	2.9	0.0	0.0
0.05	100	100	100	100	100	6.2	100	100	89.7	51.8	11.9	6.1	4.4	4.1	3.7	0.0	0.0
0.00	100	100	100	100	100	11.4	100	100	97.8	66.3	16.4	6.1	4.8	4.2	1.1	0.0	0.0
-0.05	100	100	100	100	100	100	100	100	97.5	68.4	16.2	7.5	4.9	4.3	1.1	0.0	0.0
-0.10	100	100	100	100	100	100	100	100	89.3	46.1	11.9	5.0	4.2	1.4	0.8	0.0	0.0
-0.15	100	100	100	100	100	100	12.2	51.8	83.1	44.4	3.9	3.8	1.0	1.0	0.0	0.0	0.0
-0.20	100	100	100	100	100	89.5	9.1	12.4	0.0	0.0	0.0	0.0	0.0	0.0	0.0	0.0	0.0
-0.25	100	100	100	100	100	60.0	7.4	0.0	0.0	0.0	0.0	0.0	0.0	0.0	0.0	0.0	0.0
-0.30	100	100	100	100	88.0	85.5	60.7	0.0	0.0	0.0	0.0	0.0	0.0	0.0	0.0	0.0	0.0
-0.35	100	100	100	100	93.8	100	9.8	0.0	0.0	0.0	0.0	0.0	0.0	0.0	0.0	0.0	0.0
-0.40	100	100	100	100	100	30.2	5.2	3.0	0.0	0.0	0.0	0.0	0.0	0.0	0.0	0.0	0.0
-0.45	100	100	100	100	100	4.9	19.4	17.6	0.0	0.0	0.0	0.0	0.0	0.0	0.0	0.0	0.0
-0.50	100	100	100	100	76.7	20.8	95.3	100	2.9	0.0	0.0	0.0	0.0	0.0	0.0	0.0	0.0
-0.55	88.4	84.3	24.0	24.1	90.8	58.6	100	100	19.5	0.0	0.0	0.0	0.0	0.0	0.0	0.0	0.0
-0.60	2.7	16.0	18.0	11.0	49.6	88.6	100	100	40.5	0.0	0.0	0.0	0.0	0.0	0.0	0.0	0.0
-0.65	11.1	15.8	15.7	21.5	7.6	89.7	100	100	93.4	0.0	0.0	0.0	0.0	0.0	0.0	0.0	0.0
-0.70	14.4	15.3	13.0	18.8	18.3	100.0	100	100	27.6	0.0	0.0	0.0	0.0	0.0	0.0	0.0	0.0
-0.75	15.0	20.1	15.3	17.8	26.7	73.7	100	100	0.0	0.0	0.0	0.0	0.0	0.0	0.0	0.0	0.0
-0.80	12.6	13.0	8.0	3.2	8.1	12.4	97.0	59.8	0.0	0.0	0.0	0.0	0.0	0.0	0.0	0.0	0.0
-0.85	9.0	8.1	3.0	2.1	5.7	3.3	7.9	2.0	0.0	0.0	0.0	0.0	0.0	0.0	0.0	0.0	0.0
-0.90	6.9	5.4	2.4	0.0	5.4	1.0	1.1	0.8	0.0	0.0	0.0	0.0	0.0	0.0	0.0	0.0	0.0
-0.95	4.0	3.3	1.7	0.0	0.8	0.9	1.8	1.5	1.8	0.7	0.0	0.0	0.0	0.0	0.0	0.0	0.0
-1.00	3.6	2.4	1.1	0.0	0.0	1.1	3.6	3.8	3.9	1.1	0.0	0.0	0.0	0.0	0.0	0.0	0.0
-1.05	7.1	4.4	1.9	0.0	1.1	2.3	6.4	6.6	5.8	1.9	0.0	0.0	0.0	0.0	0.0	0.0	0.0
-1.10	7.6	5.0	1.1	0.0	1.0	3.4	7.7	9.5	9.7	3.4	0.8	0.0	0.0	0.0	0.0	0.0	0.0
-1.15	6.9	3.0	1.6	0.0	0.7	1.6	6.6	5.0	6.3	0.9	0.0	0.0	0.0	0.0	0.0	0.0	0.0
-1.20	10.4	4.4	2.5	0.8	0.0	0.9	2.7	3.8	3.2	1.4	0.0	0.0	0.0	0.0	0.0	0.0	0.0
-1.25	5.4	3.8	1.9	0.8	0.0	0.8	2.4	2.9	2.6	1.0	0.0	0.0	0.0	0.0	0.0	0.0	0.0
-1.30	1.5	1.3	0.9	1.1	0.0	0.8	2.5	3.6	2.1	0.9	0.0	0.0	0.0	0.0	0.0	0.0	0.0
-1.35	1.9	1.6	1.1	2.1	0.8	1.1	2.9	3.4	3.4	3.6	0.0	0.0	0.0	0.0	0.0	0.0	0.0
-1.40	2.7	1.6	0.0	0.0	2.5	4.6	6.6	8.4	6.8	3.2	0.0	0.0	0.0	0.0	0.0	0.0	0.0
-1.45	0.0	0.0	0.0	0.0	0.8	1.1	3.8	3.9	4.5	2.8	0.0	0.0	0.0	0.0	0.0	0.0	0.0
-1.50	0.0	0.0	0.0	0.7	3.7	1.9	4.3	4.2	5.4	12.8	0.0	0.0	0.0	0.0	0.0	0.0	0.0
-1.55	0.0	0.0	0.0	0.0	0.8	1.9	2.8	3.4	1.3	0.0	0.0	0.0	0.0	0.0	0.0	0.0	0.0
-1.60	0.0	0.0	0.0	0.0	0.0	0.0	0.0	0.0	0.0	0.0	0.0	0.0	0.0	0.0	0.0	0.0	0.0

airbag to 1.1 atm. instead of 1.0 atm (i.e. the environment air pressure). Modification A2 is to add a second airbag at the front of the RA3 UAS, with 1.1 atm pressure for both airbags. For these two modifications, the FE model for the airbag design has been adapted, and subsequent novel dynamical simulations have been conducted to assess $A_{impact} \bullet \mathbb{P}\{F|impact\}$ for cases A1 and A2. As expected, under 0 m/s wind, modifications A1 and A2 perform similar than the original airbag design (case A). However, under 4 m/s wind, modifications A1 and A2 are shown to be very effective in reducing the assessed Q value; up to an extra reduction factor 5.5 x for A2 relative to case A, and a factor 19 x relative to case C. Above 4 m/s wind the risk reducing effect steadily decreases, to an extra reduction factor 1.5 x under 10 m/s wind for A2 relative to case A, and a factor 1.9 x for A2 relative to case C.

For the specific RA3 parcel delivery UAS this means that ground TPR can be reduced by an order in magnitude through equipping it with deployable parachute and airbag. This improvement would make it possible to safely deliver parcels in urban areas, under the condition that delivery under strong wind conditions is avoided.

There also are valuable directions for follow-on research. So far, we have assumed that in case A, the probability of deployment of parachute and airbag is 100 %. However, in reality a system has to detect the need for deployment of parachute and airbag, and such system will not realize below 100 %. Moreover, such a system may lead to false detections, resulting in erroneous deployments of parachute and airbag. The performance of such detection system, and its effect on the product $A_{impact} \bullet \mathbb{P}\{F|impact\}$ should also be modelled and evaluated during the UAS design phase. This detection system research has to be completed in support of the certification of the current RA3 parcel delivery UAS design with deployable parachute and airbag against standing regulation for specific operations in rural areas.

Table 16
$\mathbb{P}\{F|\Delta\}$ (%), for case A2 (1.1 atmosphere pressure in bottom and side airbag), as a function of cross offset $\Delta_\neg$ and along offset $\Delta_\parallel$, under $10m/s$ horizontal wind. Impact velocity $|v| = 12.5m/s$, descent angle $\psi = 37^\circ$, face direction $\varphi = 0^\circ$. Red line shows the boundary outside which the UAS does not touch human body. The results are shown for positive cross offset $\Delta_\neg$ only, as the results are symmetrical for negative cross offset $\Delta_\neg$. Numerical integration, using Eq. (4.5), yields $Q = 0.452m^2$.

Along offset $\Delta_\parallel$ (m) \ Cross offset $\Delta_\neg$ (m)	0.00	0.05	0.10	0.15	0.20	0.25	0.30	0.35	0.40	0.45	0.50	0.55	0.60	0.65	0.70	0.75	0.80
0.75	0.0	0.0	0.0	0.0	0.0	0.0	0.0	0.0	0.0	0.0	0.0	0.0	0.0	0.0	0.0	0.0	0.0
0.70	0.0	0.0	0.0	0.0	0.0	0.0	3.3	2.7	0.0	0.0	0.0	0.0	0.0	0.0	0.0	0.0	0.0
0.65	7.8	7.3	0.0	0.0	0.0	3.8	3.6	0.0	0.0	0.0	0.0	0.0	0.0	0.0	0.0	0.0	0.0
0.60	6.5	6.4	6.4	5.3	0.0	3.6	3.4	2.7	0.0	0.0	0.0	0.0	0.0	0.0	0.0	0.0	0.0
0.55	5.4	5.4	5.6	4.7	3.9	3.3	3.1	2.7	0.0	0.0	0.0	0.0	0.0	0.0	0.0	0.0	0.0
0.50	4.4	5.9	5.0	4.6	4.0	3.0	2.9	2.8	0.0	0.0	0.0	0.0	0.0	0.0	0.0	0.0	0.0
0.45	4.4	4.4	4.3	4.2	3.8	3.2	3.0	2.8	0.0	0.0	0.0	0.0	0.0	0.0	0.0	0.0	0.0
0.40	4.7	4.7	4.6	4.3	3.8	3.3	3.0	2.8	0.0	0.0	0.0	0.0	0.0	0.0	0.0	0.0	0.0
0.35	5.2	5.0	4.9	4.5	4.0	3.5	3.1	2.8	0.0	0.0	0.0	0.0	0.0	0.0	0.0	0.0	0.0
0.30	6.8	7.0	6.9	5.2	4.1	3.6	3.1	2.8	0.0	0.0	0.0	0.0	0.0	0.0	0.0	0.0	0.0
0.25	10.1	13.0	9.2	13.9	4.0	3.6	3.1	2.8	0.0	0.0	0.0	0.0	0.0	0.0	0.0	0.0	0.0
0.20	11.6	16.8	83.1	71.8	4.8	3.5	3.3	5.7	0.0	0.0	0.0	0.0	0.0	0.0	0.0	0.0	0.0
0.15	10.5	10.9	100	100	91.7	3.4	19.8	89.3	9.9	2.3	4.7	4.2	3.8	3.4	0.0	0.0	0.0
0.10	35.8	47.3	100	100	100	4.0	100	100	49.5	38.8	5.8	4.5	4.4	4.0	2.9	0.0	0.0
0.05	100	100	100	100	100	6.2	100	100	89.7	51.8	11.9	6.1	4.4	4.1	3.7	0.0	0.0
0.00	100	100	100	100	100	11.4	100	100	97.8	66.3	16.4	6.1	4.8	4.2	1.1	0.0	0.0
-0.05	32.2	84.8	86.7	100	100	99.7	100	100	97.5	68.4	16.2	7.5	4.9	4.3	1.1	0.0	0.0
-0.10	5.6	9.8	8.8	9.9	31.9	91.9	100	100	89.3	46.1	11.9	5.0	4.2	1.4	0.8	0.0	0.0
-0.15	6.7	13.9	10.3	6.5	6.8	21.4	12.2	51.8	83.1	44.4	3.9	3.8	1.0	1.0	0	0.0	0.0
-0.20	9.5	13.1	6.9	5.0	50.8	54.7	9.1	12.4	0.0	0.0	0.0	0.0	0.0	0.0	0.0	0.0	0.0
-0.25	9.8	8.2	5.7	5.3	68.3	41.4	7.4	0.0	0.0	0.0	0.0	0.0	0.0	0.0	0.0	0.0	0.0
-0.30	7.1	6.4	5.4	70.1	66.8	85.5	60.7	0.0	0.0	0.0	0.0	0.0	0.0	0.0	0.0	0.0	0.0
-0.35	5.9	5.6	5.0	78.0	86.4	100	9.8	0.0	0.0	0.0	0.0	0.0	0.0	0.0	0.0	0.0	0.0
-0.40	5.3	5.1	4.8	32.6	100	30.2	5.2	3.0	0.0	0.0	0.0	0.0	0.0	0.0	0.0	0.0	0.0
-0.45	4.7	4.8	4.5	4.6	100	4.9	19.4	17.6	0.0	0.0	0.0	0.0	0.0	0.0	0.0	0.0	0.0
-0.50	4.3	4.3	3.9	3.9	76.7	14.5	95.3	100	2.9	0.0	0.0	0.0	0.0	0.0	0.0	0.0	0.0
-0.55	4.0	3.9	3.6	3.4	76.3	58.4	100	100	19.5	0.0	0.0	0.0	0.0	0.0	0.0	0.0	0.0
-0.60	2.7	3.6	3.3	3.2	34.0	88.6	100	100	40.5	0.0	0.0	0.0	0.0	0.0	0.0	0.0	0.0
-0.65	11.1	15.8	15.7	21.5	7.6	89.7	100	100	93.4	0.0	0.0	0.0	0.0	0.0	0.0	0.0	0.0
-0.70	14.4	15.3	13.0	18.8	18.3	100	100	100	27.6	0.0	0.0	0.0	0.0	0.0	0.0	0.0	0.0
-0.75	15.0	20.1	15.3	17.8	26.7	73.7	100	100	0.0	0.0	0.0	0.0	0.0	0.0	0.0	0.0	0.0
-0.80	12.6	13.0	8.0	3.2	8.1	12.4	97.0	59.8	0.0	0.0	0.0	0.0	0.0	0.0	0.0	0.0	0.0
-0.85	9.0	8.1	3.0	2.1	5.7	3.3	7.9	2.0	0.0	0.0	0.0	0.0	0.0	0.0	0.0	0.0	0.0
-0.90	6.9	5.4	2.4	0.0	5.4	1.0	1.1	0.8	0.0	0.0	0.0	0.0	0.0	0.0	0.0	0.0	0.0
-0.95	4.0	3.3	1.7	0.0	0.8	0.9	1.8	1.5	1.8	0.7	0.0	0.0	0.0	0.0	0.0	0.0	0.0
-1.00	3.6	2.4	1.1	0.0	0.0	1.1	3.6	3.8	3.9	1.1	0.0	0.0	0.0	0.0	0.0	0.0	0.0
-1.05	7.1	4.4	1.9	0.0	1.1	2.3	6.4	6.6	5.8	1.9	0.0	0.0	0.0	0.0	0.0	0.0	0.0
-1.10	7.6	5.0	1.1	0.0	1.0	3.4	7.7	9.5	9.7	3.4	0.8	0.0	0.0	0.0	0.0	0.0	0.0
-1.15	6.9	3.0	1.6	0.0	0.7	1.6	6.6	5.0	6.3	0.9	0.0	0.0	0.0	0.0	0.0	0.0	0.0
-1.20	10.4	4.4	2.5	0.8	0.0	0.9	2.7	3.8	3.2	1.4	0.0	0.0	0.0	0.0	0.0	0.0	0.0
-1.25	5.4	3.8	1.9	0.8	0.0	0.8	2.4	2.9	2.6	1.0	0.0	0.0	0.0	0.0	0.0	0.0	0.0
-1.30	1.5	1.3	0.9	1.1	0.0	0.8	2.5	3.6	2.1	0.9	0.0	0.0	0.0	0.0	0.0	0.0	0.0
-1.35	1.9	1.6	1.1	2.1	0.8	1.1	2.9	3.4	3.4	3.6	0.0	0.0	0.0	0.0	0.0	0.0	0.0
-1.40	2.7	1.6	0.0	0.0	2.5	4.6	6.6	8.4	6.8	3.2	0.0	0.0	0.0	0.0	0.0	0.0	0.0
-1.45	0.0	0.0	0.0	0.0	0.8	1.1	3.8	3.9	4.5	2.8	0.0	0.0	0.0	0.0	0.0	0.0	0.0
-1.50	0.0	0.0	0.0	0.7	3.7	1.9	4.3	4.2	5.4	12.8	0.0	0.0	0.0	0.0	0.0	0.0	0.0
-1.55	0.0	0.0	0.0	0.0	0.8	1.9	2.8	3.4	1.3	0.0	0.0	0.0	0.0	0.0	0.0	0.0	0.0
-1.60	0.0	0.0	0.0	0.0	0.0	0.0	0.0	0.0	0.0	0.0	0.0	0.0	0.0	0.0	0.0	0.0	0.0

A second direction for follow-on research is to complement the assessment of ground TPR with an uncertainty and sensitivity analysis of model parameter assumptions. So far, this direction has hardly received attention in UAS literature. A recent exception is [Badea et al., 2024], who study varying wind conditions faced by UAS flying in urban environment. This follow-on research direction does not preclude that the current RA3 parcel delivery UAS design with deployable parachute and airbag can be implemented and certified against standing regulation for specific operations in rural areas.

A third direction for follow-on research is to further study the integration of complementary injury criteria for HIC, Nij, and VC, through Eq. (3.1). This equation is based on the assumption that contributions to PoF by different injury types are independent. However, for the specific application in the current paper, the local contributions from Nij and VC are so much smaller than those for HIC, that the independence assumption plays a negligible role.

A fourth direction for follow-on research is to enhance the fidelity of airbag gas modelling. In the current study MADYMO's uniform pressure (UP) model has been adopted, which inherently simplifies gas behaviour within the airbag. For broader UAS operational scenarios it would be valuable to also investigate high-fidelity gas dynamics model, e.g. MADYMO's gasflow model. This allows to investigate the effect of higher collision velocities, airbag partial inflation or actively venting airbag designs, where non-uniform gas dynamics may significantly influence injury outcomes. Such high-fidelity modelling can be supported by acquiring spatially and temporally resolved experimental data.

From a more general UAS research perspective, the paper has delivered the following specific novelties:

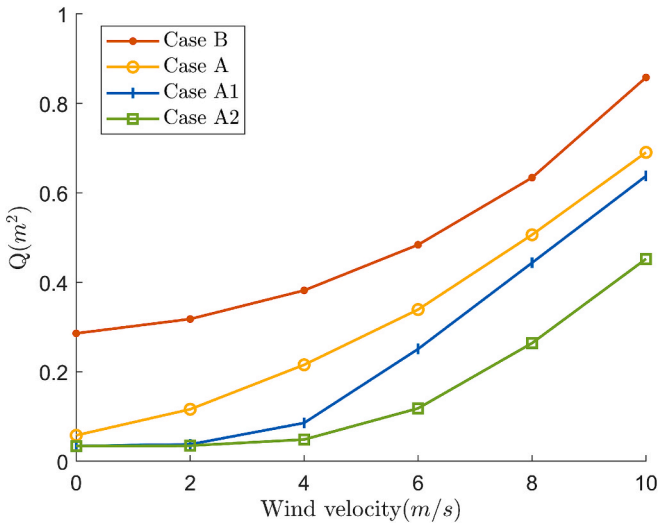

Fig. 13. Q as a function of horizontal wind velocity, for case B (no airbag), case A (bottom airbag, 1 atm.), case A1 (bottom airbag at 1.1 atm.) and A2 (bottom and front airbags at 1.1 atm.).

Table 17
Q for cases C, B, A, A1, and A2 for $0m/s$, $4m/s$ and $10m/s$ wind.

Case	0 m/s wind	4 m/s wind	10 m/s wind
C (no parachute, no airbag)	0.849 m^2	0.853 m^2	0.859 m^2
B (parachute, no airbag)	0.256 m^2	0.382 m^2	0.858 m^2
A (parachute, 1 atm bottom airbag)	0.031 m^2	0.216 m^2	0.677 m^2
A1 (parachute, 1.1 atm bottom airbag)	0.026 m^2	0.086 m^2	0.638 m^2
A2 (parachute, 1.1 atm bottom & front airbag)	0.025 m^2	0.049 m^2	0.452 m^2

– First time that a dynamical simulation model of an airbag is used in ground TPR assessment.
– First time that the method of [Jiang et al., 2024] is shown to work well for a parcel delivery UAS that is equipped with deployable parachute and airbag.
– First time that a paper demonstrates effective feedback to UAS design of dynamical modelling and simulation-based assessment of the product $A_{impact} \bullet \mathbb{P}\{F|impact\}$.

The remarkable novel results obtained for the RA3 design, also forms a motivation to apply the dynamical modelling and simulation method of [Jiang et al., 2024] and to feedback the results to the design of other quadcopter UAS and to other UAS types such as fixed wing UAS, e.g. [Zipline, 2023] and VTOL systems, e.g. [Ehang, 2023; Wing, 2023].

CRediT authorship contribution statement

Chengpeng Jiang: Writing – review & editing, Writing – original draft, Visualization, Validation, Software, Methodology, Formal analysis, Conceptualization. **Henk Blom:** Writing – review & editing, Writing – original draft, Validation, Supervision, Formal analysis. **Borrdephong Rattanagraikanakorn:** Writing – review & editing, Software, Resources, Data curation.

Declaration of competing interest

The authors declare that they have no known competing financial interests or personal relationships that could have appeared to influence the work reported in this paper.

Acknowledgement

The authors gratefully acknowledge Hangzhou Antwork Technology Co., Ltd. for providing the drone specifications and the physical prototype essential for this study. We are also grateful to the School of Materials Science and Engineering, Zhejiang University for assissting the drone prototype test.

Appendix A. . MBS model of RA3

Body masses and segments

The seven rigid masses and their connections in the MBS model for RA3 are shown in Fig. A1a. Bodies 1–6 are connected with Joints 1–6 to Body 0 as shown in Fig. A1b. Joints 1–6 are universal joints, for which Cardan restraints (torsional spring parallel with a damper) are used to account for force deflections from structure deformations.

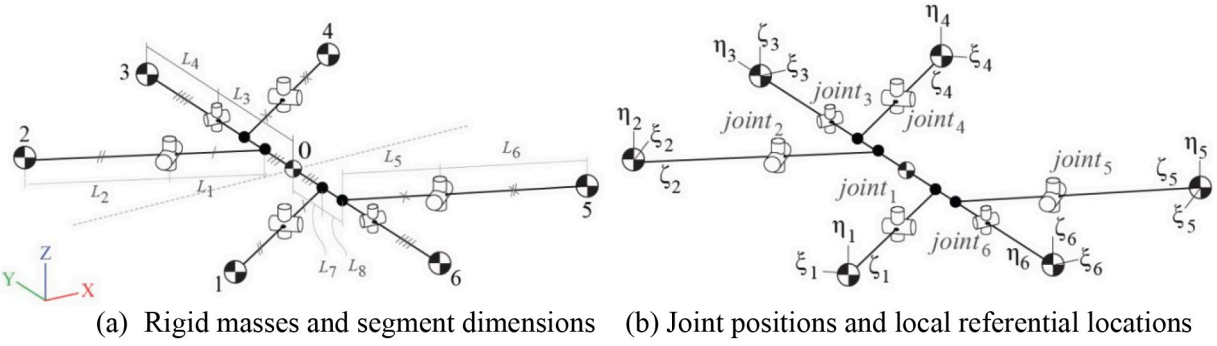

(a) Rigid masses and segment dimensions (b) Joint positions and local referential locations

Fig. A1. Skeleton of the MBS model of RA3 UAS showing rigid masses, joints, and restraints.

In Tables A1 and A2, RA3 UAS model segment dimensions, masses and moment of inertia are given. Geometrical dimensions and masses are obtained from physical measurements of the UAS parts. Moment of inertia of each body parts are measured using bifilar test.

Table A1
Geometrical dimensions of the RA3 UAS.

Segment	Length(m)	Segment	Length(m)
L1	0.181	L5	0.143
L2	0.409	L6	0.412
L3	0.173	L7	0.089
L4	0.456	L8	0.141

Table A2
Mass and moment of inertial of each body.

Body part	Mass (g)		Moment of inertia ($kg*m^2$)					
Body 0 (Main frame)	m0	11974.4	$I_{XX}0$	0.499	$I_{YY}0$	0.382	$I_{ZZ}0$	0.771
Body 1 (Arm 1)	m1	502	$I_{XX}1$	0.002	$I_{YY}1$	0.001	$I_{ZZ}1$	0.003
Body 2 (Arm 2)	m2	502	$I_{XX}2$	0.002	$I_{YY}2$	0.001	$I_{ZZ}2$	0.003
Body 3 (Arm 3)	m3	515.5	$I_{XX}3$	0.003	$I_{YY}3$	0.001	$I_{ZZ}3$	0.004
Body 4 (Arm 4)	m4	522.5	$I_{XX}4$	0.003	$I_{YY}4$	0.001	$I_{ZZ}4$	0.004
Body 5 (Arm 5)	m5	522.5	$I_{XX}5$	0.003	$I_{YY}5$	0.001	$I_{ZZ}5$	0.004
Body 6 (Arm 6)	m6	515.5	$I_{XX}6$	0.003	$I_{YY}6$	0.001	$I_{ZZ}6$	0.004

Arm stiffness measurement

The stiffness of an RA3 arm is quantified as the moment M as a function of angular displacement θ. Using quasi-static compression test (Fig. A2), force F- displacement d curve is firstly obtained, and the moment M- angular displacement θ curve (Fig. A3) is subsequently generated using $M = F \times L$ and $\theta = d/L$, where L is the length of arm. Due to that arms 1–6 use the same carbon fibre material and same type of aluminium connector to the mainframe, they have the same torsional stiffness.

Fig. A2. Quasi-static compression test of an arm of RA3 UAS.

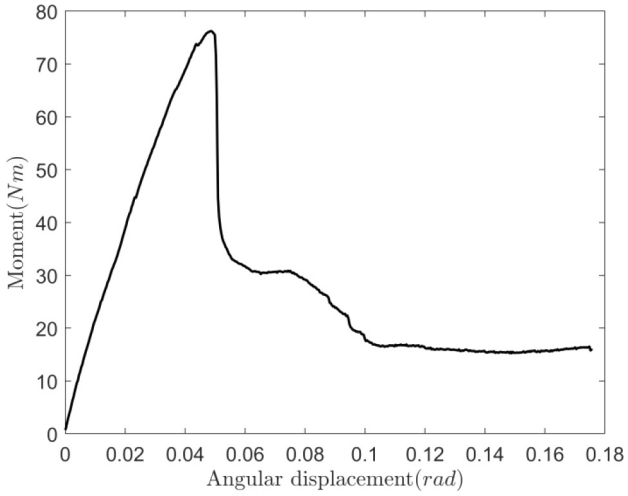

Fig. A3. Moment $M-$angular displacement θ curve of arms 16 of RA3 UAS.

Appendix B. . Contact model of RA3 with human

Properties of human scalp and RA3 UAS material are in Table B1. Material property of the RA3 UAS carbon fibre is obtained from online source [Matweb, 2022]. The head contact surface is assumed to have the characteristics of human head scalp. The material property of human head scalp is obtained from [Falland-Cheung et al., 2018].

Table B1
Properties of human head scalp and RA3 UAS material.

Materials	Young's modulus (*Pa*)	Poisson ratio	Radius (*m*)	Yield strength (*Pa*)
Human head scalp	$2.23^{*}10^{7}$	0.29	0.0875	$3.42^{*}10^{6}$
Carbon fibre	$5.48^{*}10^{10}$	0.34	0.03 (for arm)	$5.93^{*}10^{7}$

The corresponding contact compliance curves for the RA3 main frame and arms are obtained using the Hertz elastic contact model [Brake, 2012] as shown in Fig. B1.

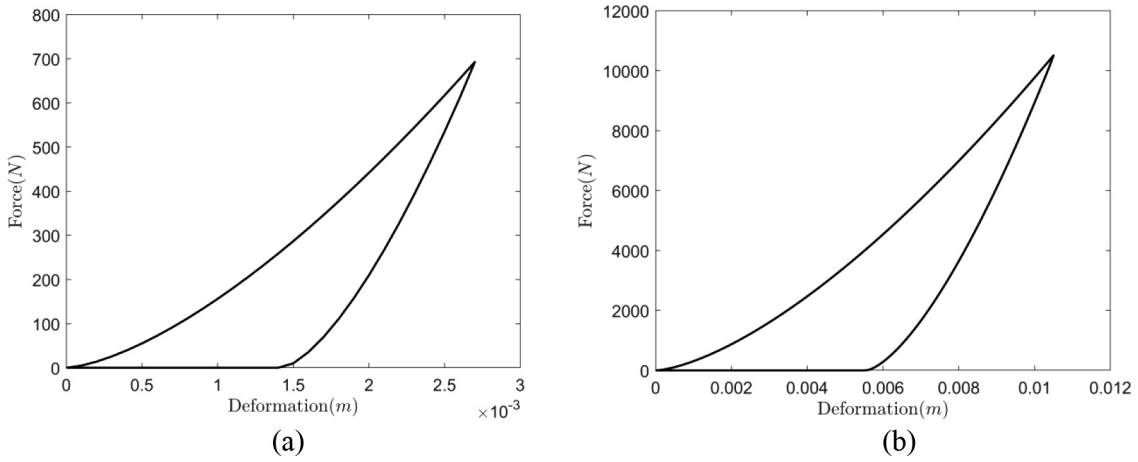

Fig. B1. Contact compliance curves for RA3 UAS-human head contact. (a) RA3 arm contact (b) RA3 mainframe contact.

The contact compliance curve for cargo box is obtained using ellipsoid-foam contact model [Chou et al., 1994] as shown in Fig. B2. This contact compliance curve is obtained as a product of contact area and contact stress. The contact area curve and contact stress curve are shown in Figs. B3 and B4. The contact area curve shows the size of cross-sectional area as a function of deformation of cargo box impacting human head shape model as a sphere with 0.0875 *m* radius. The contact stress curves for foam loading–unloading are from [Avalle et al., 2018] for EPP foam of density 70 kg/m^3.

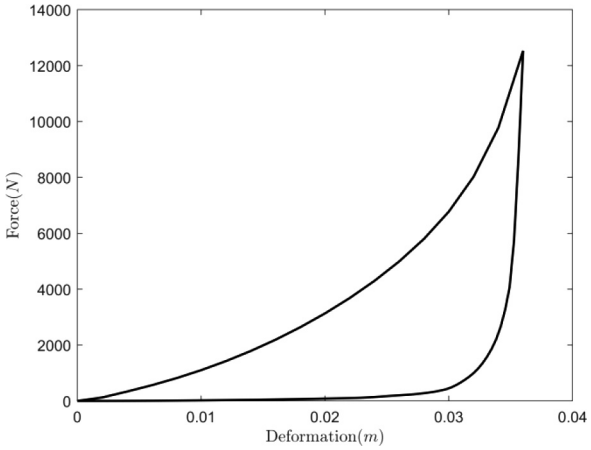

Fig. B2. Contact compliance curve for RA3 cargo box-human head contact.

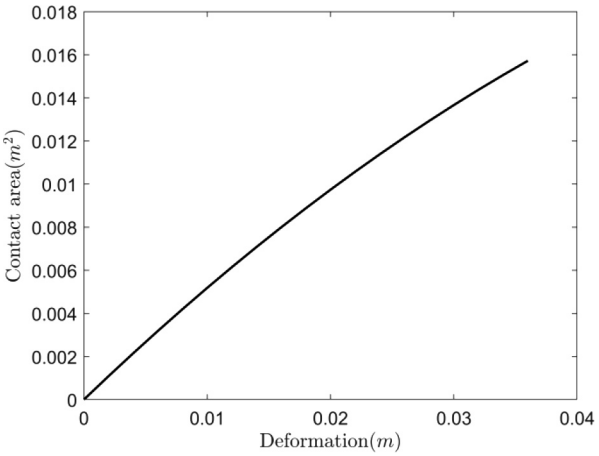

Fig. B3. Contact area – deformation curve for RA3 cargo box-human head contact.

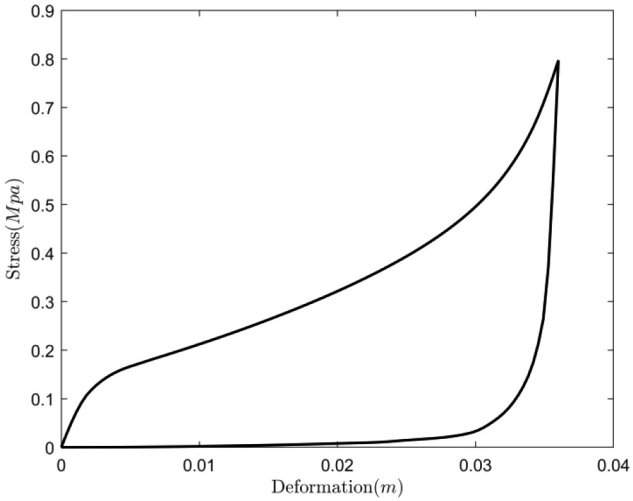

Fig. B4. Contact stress – deformation curve for RA3 cargo box-human head contact [Avalle et al., 2018].

Appendix C. . Conversion of human injury criteria to probability of fatality

- **Head Injury Criterion**

The *HIC* equation is defined as follows [Hutchinson et al., 1998]:

$$HIC = \max_{t_1,t_2}\left\{\frac{1}{(t_1-t_2)^{3/2}}\left[\int_{t_1}^{t_2} a(t)dt\right]^{5/2}\right\} \tag{C.1}$$

where $a(t)$ is the head acceleration observed at centre of mass of head as a function of time t, t_1 and t_2 are two time points during the impact. There are two range limits for $t_1 - t_2$, which are 15 *ms* and 36 *ms*. $t_1 - t_2$ can be seen as the impact time during which the peak impact energy is transferred from UAS to human head. Common practice for head injury simulation in a car crash accident is to use a 15 *ms* time range limit; this time range is also adopted for UAS impact on human head.

The *HIC* can be converted to percentage of life-threatening injury using the U.S. ISO Delegation recommended curve [Tyrell et al., 1995] in Fig. C1. The percentage of life-threatening injury is equivalent to the Probability of Fatality (PoF).

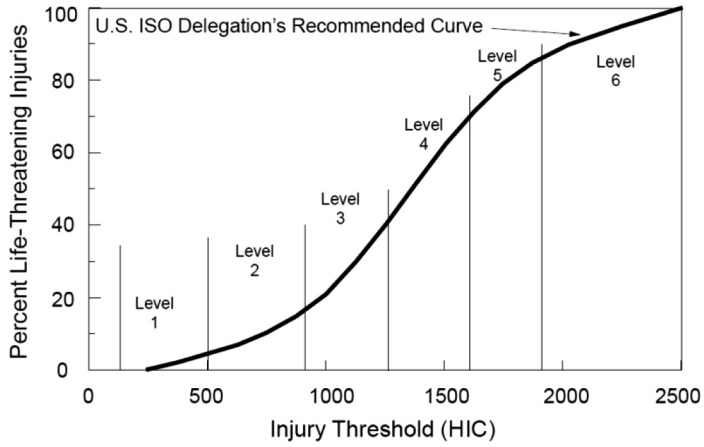

Fig. C1. Convention of HIC to percentage of life-threatening injury [Tyrell et al., 1995].

- **Neck Injury Criterion**

For the four types of neck injury N_{ij}, namely N_{TF}, N_{TE}, N_{CF}, N_{CE}, the equation is:

$$N_{ij} = \left|\frac{F_Z}{F_{int}}\right| + \left|\frac{M_Y}{M_{int}}\right| \tag{C.2}$$

where F_Z is the upper neck Z-axis loading force, M_Z is the upper neck Y-axis loading moment, F_{int} and M_{int} are the corresponding critical intercept value of load for normalization.

For neck injury, the highest of the four assessed N_{ij} values is converted to Probability of Fatality (PoF). In doing so we use the transformation curve in Fig. C2, which curve provides an upper bound in PoF as a function of assessed N_{ij} value.

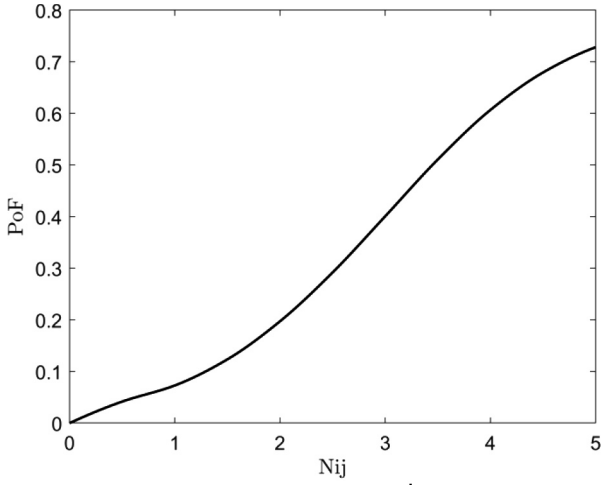

Fig. C2. Probability of Fatality P{$F|N_{ij}$} as a function of N_{ij}.

Fig. C2 is obtained below, following a sequence of four steps. The first step is to adopt the AIS probability curve fittings as function of N_{ij} levels by [Eppinger et al., 1999] on realistic injury data; these are given in Fig. C3a. As can be seen in Fig. C3a, the left and right parts of these curve fittings sometimes show unrealistic patterns. The second step is to resolve these unrealistic patterns by applying the following two logical to the curves in Fig. C3a: i) $\mathbb{P}\{AIS|N_{ij}=0\}=0$; and ii) $\mathbb{P}\{AIS\geq k|N_{ij}\}\geq\mathbb{P}\{AIS\geq k+1|N_{ij}\}$ for $k=4,3,2$ and all N_{ij}. Application of these conditions to the curves in Fig. C3a yields the curves in Fig. C3b.

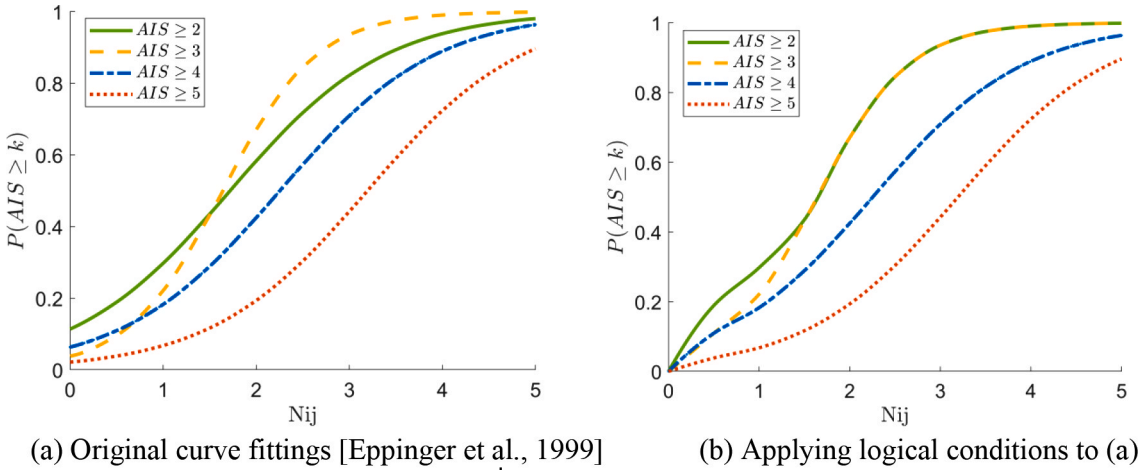

Fig. C3. as a function of N_{ij} for $k = 2,\ldots.5$.

The third step is to transform each of the four AIS curves in Fig. C3b, to PoF curves. For this transformation we adopt the conversion by [Gennarelli and Wodzin, 2006], to transform AIS levels to probability of fatality; this curve is shown in Fig. C4.

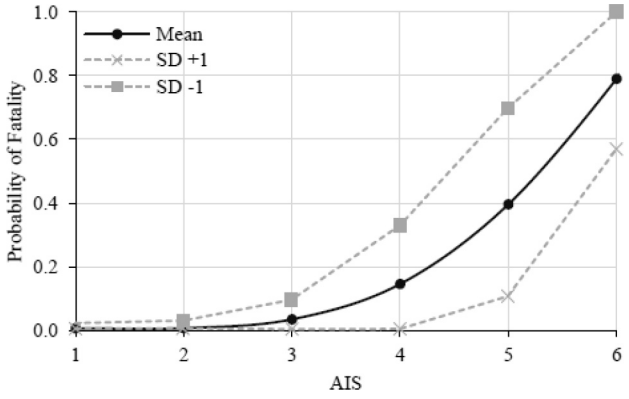

Fig. C4. Conversion of AIS to probability of fatality [Gennarelli and Wodzin, 2006].

The fourth step is to combine the four $\mathbb{P}\{AIS \geq k|N_{ij}\}, k = 1,2,3,4$, curves in Fig. 3C.b with the conversion curve $\mathbb{P}\{F|AIS = k\}$ in Fig. C4, to a single PoF curve as function of N_{ij}. For this fourth step we develop the following probabilistic analysis:

$$\mathbb{P}\{F|N_{ij}\} = \sum_{k=2}^{4}\left[\mathbb{P}\{F|AIS = k\}\mathbb{P}\{AIS = k|N_{ij}\}\right] + \mathbb{P}\{F|AIS \geq 5\}\mathbb{P}\{AIS \geq 5|N_{ij}\}$$

$$\leq \sum_{k=2}^{4}\left[\mathbb{P}\{F|AIS = k\}\mathbb{P}\{AIS = k|N_{ij}\}\right] + \mathbb{P}\{F|AIS = 6\}\mathbb{P}\{AIS \geq 5|N_{ij}\} \quad \text{(C.3)}$$

$$= \sum_{k=2}^{4}\left[\mathbb{P}\{F|AIS = k\}\left(\mathbb{P}\{AIS \geq k|N_{ij}\} - \mathbb{P}\{AIS \geq k+1|N_{ij}\}\right)\right] + \mathbb{P}\{F|AIS = 6\}\mathbb{P}\{AIS \geq 5|N_{ij}\}$$

where $\mathbb{P}\{AIS \geq k|N_{ij}\}$ is quantified in Fig. C3b, and $\mathbb{P}\{F|AIS = k\}$ is quantified in Fig. C4. Subsequent evaluation of the latter inequality, by using the curves in Figs. C3b and C4, yields the curve in Fig. C2.

- **Viscous Criterion (VC)**

The VC injury level *VC* for a specific body part is generated as follows:

$$VC = \max_{t,r}[V(t,r) \times C(t,r)] \quad \text{(C.4)}$$

where $V(t,r)$ is the deformation speed of the body part at moment t and location r. $C_B(t,r)$ is the compression in the percentage of the thickness of the body part at moment t and location r.

The VC injury level *VC* is converted to PoF $\mathbb{P}(F|VC)$ using the following equation:

$$\mathbb{P}\{F|VC\} = \mathbb{P}(F|AIS)\mathbb{P}(AIS|VC) \quad \text{(C.5)}$$

The curve for $\mathbb{P}(AIS|VC)$ is shown in Fig. C5 [Sturdivan et al., 2004] which is based on blunt impact experiment on cadavers [Cavanaugh et al., 1990;

Viano et al., 1989]. For $\mathbb{P}(F|AIS)$ use is made of the curve in Fig. C4. Combining the curves in Figs. C4 and C5, by using Eq. (C5), yields the curve in Fig. C6 for conversion of VC injury level to PoF value.

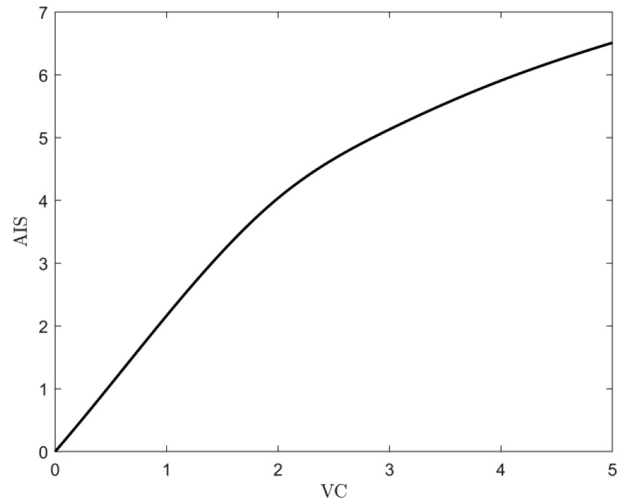

Fig. C5. Conversion of VC injury level to AIS level [Sturdivan et al., 2004].

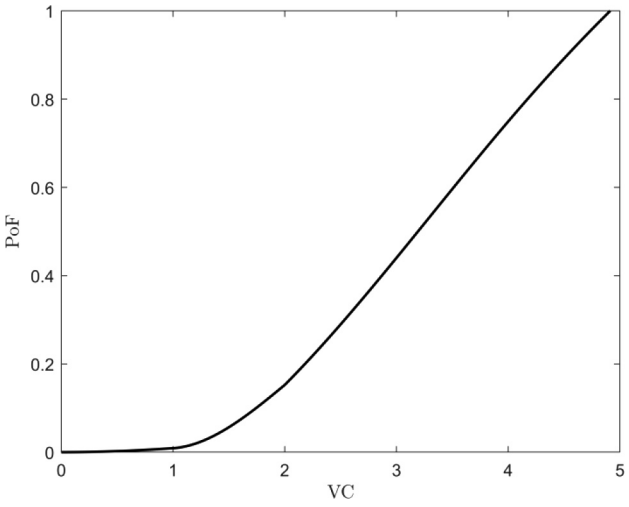

Fig. C6. Conversion of VC injury level to PoF.

Appendix D. . Existing models for assessment of A_{impact} and $\mathbb{P}\{F|impact\}$ for various UAS types

This subsection summarizes the parametric models for A_{impact} and $\mathbb{P}\{F|impact\}$ that apply to a wide variety of UAS, including RA3 without airbag. Common practice, e.g. [Melnyk et al., 2014; Primatesta et al., 2020], is to assume that A_{impact} and $\mathbb{P}\{F|impact\}$ are independent.

Parametric models for A_{impact}

The widely used models for A_{impact} are Gliding area [RCC, 2001], Planform area [Weibel and Hansman, 2004], and Maximum Take Off Weight (MTOW) based area [Ale and Piers, 2000].

The Gliding area model of RCC [RCC, 2001] satisfies:

$$A_{impact} = (Width_{UAS} + 2R_P)\left(\frac{H_P}{tan(\psi)} + D_{Slide} + Length_{UAS} + 2R_P\right) \tag{D.1}$$

with $Width_{UAS}$ the dimension of the UAS, $2R_P$ and H_P the diameter and height of person, ψ the UAS descent angle, D_{Slide} the sliding distance until a safe speed (no longer injuries to people) is reached.

The planform area model [Weibel and Hansman, 2004] only considers the size of the aircraft:

$$A_{impact} = Width_{UAS} \cdot Length_{UAS} \tag{D.2}$$

The MTOW based area model satisfies [Ale and Piers, 2000]: $A_{impact} = c_{Fit} m_{MTOW}$, with m_{MTOW} the Maximum Take-Off Weight in kg, and the statistically fitted coefficient value $c_{Fit} = 0.2$ m^2/kg.

Parametric models for $\mathbb{P}\{F|impact\}$

For $\mathbb{P}\{F|impact\}$ the widely used models are Range Commanders Council (RCC) [RCC, 2001], Blunt Criteria (BC) [Magister, 2010] and Area Weight Kinetic Energy (AWKE) models [Arterburn, 2017].

The RCC [2001] fatality risk curve is a function of kinetic energy of UAS at moment of impact of human body, and is based on a weighted average of the fatality risk curves that are obtained through statistical analysis of a military database of effects of blast, debris on human body parts [Feinstein et al., 1968]:

$$\mathbb{P}\{F|impact\} = Z(\frac{lnE_{imp} - lna}{b}) \tag{D.3}$$

where Z is the cumulative standard normal distribution, and E_{imp} is the impact energy. Hence Z defines an S-shaped curve that starts at probability zero for $E_{imp} = 0$, reaches probability $1/2$ for $E_{imp} = a$ and asymptotically goes to probability 1 for large E_{imp}. The parameter values for a and b for a standard male human for different body parts as shown in Table D1.

Table D1
Model parameter values for a standard male human. Source: [RCC, 2000].

Parameter	Head	Thorax	Abdomen
a(Joules)	74.8	59.8	130.6
b	0.2802	0.3737	0.4335

The AWKE model [Arterburn et al., 2017] adopts a weighted mean of the fatality probabilities for Head, Thorax and Abdomen.

Magister [2010] proposed to adopt the Blunt Criterion (BC) as basis for a human injury due to UAS impact. The basis for this approach stems from military kind of ballistic impacts on human [Sturdivan et al., 2004]. The BC injury level L_{BC} satisfies:

$$L_{BC} = ln\frac{E_{imp}}{{m_b}^{1/3} l_b D_{imp}} \tag{D.4}$$

where E_{imp} is the impact energy, m_b is the mass of the impacted body part, l_b is the thickness (in cm) of body wall of the impacted body part, D_{imp} is the diameter (in cm) of the impacting object, e.g. an impacting UAS. For thorax and abdomen, l_b depends on the body part mass:

$$l_b = {m_b}^{1/3} c_b \tag{D.5}$$

where c_b is the thickness parameter of the body part considered. Table D2 gives the parameter values adopted for BC impacts of head [CASA, 2013], and of thorax and abdomen [Sturdivan et al., 2004].

Table D2
BC model values for impact on standard male.

Parameter	Head	Thorax	Abdomen	Source
Mass ratio of body part	8 %	21 %	21 %	[Sturdivan et al., 2004]
c_b	n.a.	0.711	0.711	[Sturdivan et al., 2004]
$l_b(cm)$	1.3	n.a.	n.a.	[CASA, 2013]

Values for $\mathbb{P}\{F|impact\}$ are obtained by applying two successive mappings. First, injury level L_{BC} is converted to AIS level L_{AIS} [Bir & Viano, 2004] using:

$$L_{AIS} = 1.33 \cdot L_{BC} + 0.6 \tag{D.6}$$

Second, AIS level is converted to $\mathbb{P}\{F|impact\}$ by using the transformation curve of single injury AIS scale to probability of fatality [Gennarelli & Wodzin, 2006].

Data availability

Data will be made available on request.

References

ADVANCE, 2003. Work package 5.1, Restraint system numerical simulation of enhanced models and ALE, Deliverable D17, Draft Version 4.

Ale, B., Piers, M., 2000. The assessment and management of third party risk around a major airport. J. Hazard. Mater. 71 (1–3), 1–16.

Antwork, 2020. Parachute canopy folding structure, parachute, landing system, unmanned aerial vehicle, Chinese patent: CN111216900A.

Antwork, 2023. Antwork Introduction, URL: https://www.antwork.link/introduction.html [retrieved 24th, July 2023].

Arterburn, D., Ewing, M., Prabhu, R., Zhu, F., Francis, D., 2017. UAS Ground Collision Severity Evaluation, ASSURE Task A4 Final Report. FAA UAS Center of Excellence. , URL: https://www.assureuas.org/projects/completed/a4/ASSURE_A4.

Arterburn, D., Olivares, G. Bolte, J., Prabhu, R., Duma, S., 2019. UAS Ground Collision Severity Evaluation 2017-2019, ASSURE Task A14 Final Report. FAA, Atlantic City, NJ, URL: https://www.assureuas.org/projects/completed/a14/ASSURE_A14.

Avalle, M., Frascio, M., Monti, M., 2018. An improved model to describe the repeated loading-unloading in compression of cellular materials. Procedia Struct. Integrity 12, 19–31.

Badea, C.A., Morfin Veytia, A., Ellerbroek, J., Hoekstra, J., 2024, Urban wind measurement and modelling for U-space operations, Proc. ICRAT 2024, Singapore.

Bertrand, S., Raballand, N., Viguier, F., Muller, F., 2017. Ground Risk Assessment for Long-Range Inspection Missions of Railways by UAVs. Proceedings of 2017 International Conference on Unmanned Aircraft Systems. pages: 1343-1351. Miami, FL.

Bir, C., Viano, D.C., 2004. Design and injury assessment criteria for blunt ballistic impacts. J. Trauma Acute Care Surg. 57 (6), 1218–1224.

Blom, H.A.P., Jiang, C., Grimme, W.B.A., Mitici, M., Cheung, Y.S., 2021. Third party risk modelling of Unmanned Aircraft System operations, with application to parcel delivery service[J]. Reliab. Eng. Syst. Saf. 214, 107788.
Brake, M.R., 2012. An analytical elastic-perfectly plastic contact model. Int. J. Solids Struct. 49 (22), 3129–3141.
CASA, 2013. Human injury model for small unmanned aircraft impacts. Australian Civil Aviation Safety Authority.
Cavanaugh, J.M., Walilko, T.J., Malhotra, A., Zhu, Y., King, A.I., 1990. Biomechanical response and injury tolerance of the pelvis in twelve sled side impacts. SAE Tech. Pap. 99, 1678–1693. https://doi.org/10.4271/902305.
Cawthorne, D., 2016. Development of a Multirotor Drone Airbag. Master thesis, University of Southern Denmark, December 2016.
Chou, C.C., Lim, G.G., Sundararajan, S., Low, T.C., Prasad, P., Mitchell, J.O., 1994. Experimental validation of ellipsoid-to-foam contact model. SAE Trans. 667–678.
Clothier, R., Walker, R., Fulton, N., Campbell, D., 2007. A casualty risk analysis for unmanned aerial system (UAS) operations over inhabited areas. In: Proceedings of Proceedings of AIAC12: 2nd Australasian Unmanned Air Vehicles Conference, pp. 1–16.
Clothier, R.A., Williams, B.P., Hayhurst, K.J., 2018. Modelling the risks remotely piloted aircraft pose to people on the ground. Saf. Sci. 101, 33–47.
Disney, 2016. Impact absorption apparatus for unmanned aerial vehicle, United States Patent: US2016/0332739.
DJI, 2019. Impact protector equipment, Chinese patent: CN106029499B.
DJI, 2022. Dropsafe, URL: https://www-v1.dji.com/nl/dropsafe.html [retrieved 24th, July 2023].
EASA, 2021. Study on the societal acceptance of Urban Air Mobility in Europe, European Union Aviation Safety Agency, 19th May 2021.
Ehang, 2023. Passenger transportation and logistics, URL: https://www.ehang.com/uam/ [retrieved 20th, July 2023].
Eppinger, R., Sun, E., Bandak, F., Haffner, M., Khaewpong, N., Maltese, M., Kuppa, S., Nguyen, T., Takhounts, E., Tannous, R., Zhang, A., Saul, R., 1999. Development of improved injury criteria for the assessment of advanced automotive restraint systems: II. National Highway Traffic Safety Administration.
FAA, 2016. Operation and Certification of Small Unmanned Aircraft Systems. Department of Transportation, Washington, USA.
Falland-Cheung, L., Scholze, M., Lozano, P.F., Ondruschka, B., Tong, D.C., Brunton, P.A., Hammer, N., 2018. Mechanical properties of the human scalp in tension. J. Mech. Behav. Biomed. Mater. 84, 188–197.
Feinstein, D.I., Heugel, W.F., Kardatzke, M.L., Weinstock, A., 1968. Personnel casualty study. IIT Research Institute, Chicago, IL.
Flyfire, 2022. drone safety parachute, https://www.flyfiretech.com/ [retrieved 24th, July 2023].
Foster, J.V., Hartman, D., 2017. High-Fidelity Multi-Rotor Unmanned Aircraft System (UAS) Simulation Development for Trajectory Prediction Under Off-Nominal Flight Dynamics. Proceedings of 17th AIAA ATIO Conference. pages: 1-17. Denver, Colorado.
Gennarelli, T.A., Wodzin, E., 2006. AIS 2005: a contemporary injury scale. Injury 37 (12), 1083–1091.
Happee, R., Hoofman, M., Van den Kroonenberg, A.J., Morsink, P., Wismans, J.S.H.M., 1998. A mathematical human body model for frontal and rearward seated automotive impact loading. SAE Trans. 2720–2734.
Happee, R., Ridella, S., Nayef, A., Morsink, P., de Lange, R., Bours, R., Van Hoof, J., 2000. Mathematical human body models representing a mid-size male and a small female for frontal, lateral and rearward impact loading. In: 2020 IRCOBI Conference, pp. 67–84.
Happee, Riender, Rekveldt, M., Schoenmakers, F., 2003. Advanced airbag modelling for side airbags and OOP using MADYMO, 59-75+340.
Hutchinson, J., Kaiser, M.J., Lankarani, M., 1998. The Head Injury Criterion (HIC) functional. J. Appl. Math. Comput. 96, 1–16.
ICAO, 2011. Unmanned Aircraft Systems (UAS), Cir 328, International Civil Aviation Organization.
JARUS, 2022. JARUS guidelines on SORA-Annex F, Draft for external consultation, Edition 0.3, Joint Authorities Regulation Unmanned Systems.
JARUS, 2023. SORA v2.0 to v2.5 - Summary of changes for external consultation, EASA workshop presentation slides, February 2023.
Jiang C., Blom H.A.P., Rattanagraikanakorn B., 2024, Enhancing safety feedback to the design of small, unmanned aircraft by joint assessment of impact area and human fatality, Risk Analysis, September 2024, doi: 10.1111/risa.17649.
Klinich, K.D., Saul, R.A., Auguste, G., Backaitis, S., Kleinberger, M., 1996. Techniques for developing child dummy protection reference values, measurement, Report 00819638, National Highway Traffic Safety Administration, doi: 10.21949/1403104.
Koh, C.H., Low, K.H., Li, L., Zhao, Y., Deng, C., Tan, S.K., Chen, Y., Yeap, B.C., Li, X., 2018. Weight threshold estimation of falling UAVs (Unmanned Aerial Vehicles) based on impact energy. Transp. Res. Part C Emerging Technol. 93, 228–255. https://doi.org/10.1016/j.trc.2018.04.021.
la Cour-Harbo, A., 2019. Quantifying risk of ground impact fatalities for small unmanned aircraft. J. Intell. Robot. Syst. 93 (1), 367–384. https://doi.org/10.1007/s10846-018-0853-1.
la Cour-Harbo, A., 2020. Ground impact probability distribution for small unmanned aircraft in ballistic descent. In 2020 International Conference on Unmanned Aircraft Systems (ICUAS), September 2020, pp. 1442-1451. IEEE.
Lau, I.V., Viano, D.C., 1986. The viscous criterion—bases and applications of an injury severity index for soft tissues. SAE Trans. 672–691.
MADYMO, 2017a. MADYMO Human body models manual, Release 7.7, TASS International.
MADYMO, 2017b. MADYMO Theory manual Version 7.7, MADYMO utility manual, TASS International.
MADYMO, 2020. MATERIAL.FABRIC_SHEAR, User reference, version 2020.2.
MADYMO, 2023. Simcenter Madymo Software, URL: https://plm.sw.siemens.com/en-US/simcenter/mechanical-simulation/madymo/ [retrieved 24th, July 2023].
Magister, T., 2010. The small unmanned aircraft blunt criterion-based injury potential estimation. Saf. Sci. 48 (10), 1313–1320.
Manta Air, 2023. UAV recovery systems, URL: https://manta-air.com/ [retrieved 24th, July 2023].
Matweb, 2022. Online Materials Infomation Resource, URL: https://www.matweb.com/ [retrieved retrieved 20th, June 2022].
Melnyk, R., Schrage, D., Volovoi, V., Jimenez, H., 2014. A third-party casualty risk model for unmanned aircraft system operations. Reliab. Eng. Syst. Saf. 124, 105–116.
Parr, M.J.C., Miller, M.E., Bridges, N.R., Buhrman, J.R., Perry, C.E., Wright, N.L., 2012. Evaluation of the Nij neck injury criteria with human response data for use in future research on helmet mounted display mass properties. Proc. Human Factors Ergon. Soc. 2070–2074. https://doi.org/10.1177/1071181312561439.
Primatesta, S., Rizzo, A., la Cour-Harbo, A., 2020. Ground risk map for unmanned aircraft in urban environments. J. Intell. Robot. Syst. 97 (3), 489–509.
Rattanagraikanakorn, B., Schuurman, M., Gransden, D.I., Happee, R., De Wagter, C., Sharpanskykh, A., Blom, H.A.P., 2019. Modelling Head Injury due to Unmanned Aircraft Systems Collision: Crash Dummy vs Human Body, Proc. 19th AIAA ATIO Conf., June 2019, Dallas, TX, 10.2514/6.2019-2835.
Rattanagraikanakorn, B., Gransden, D.I., Schuurman, M., De Wagter, C., Happee, R., Sharpanskykh, A., Blom, H.A.P., 2020. Multibody system modelling of unmanned aircraft system collisions with the human head. Int. J. Crashworthiness 25 (6), 689–707.
Rattanagraikanakorn, B., 2021. Modelling Collision Consequences of Unmanned Aircraft Systems on Human, PhD thesis, Delft University of Technology, November 2021.
RCC, 2001. Range Safety criteria for Unmanned Air Vehicles, Rationale and methodology supplement. Supplement to Document 323-99, Range Commanders Council, April 2001.
SAES, 2025. Emeth P11: Defining Safety Standards for the Drone Industry, https://www.saesgetters.com/designhouse/emeth-p11-defining-safety-standards-for-the-drone-industry/ [retrieved 10th, Jan 2025].
Schmitt, K.-U., Niederer, P.F., Cronin, D.S., Morrison III, B., Muser, M.H., Walz, F., 2019. Trauma Biomechanics: An Introduction to Injury Biomechanics, 5th Edition. Springer.
Stark, D.B., Willis, A.K., Eshelman, Z., Kang, Y.S., Ramachandra, R., Bolte, J.H., McCrink, M., 2019. Human response and injury resulting from head impacts with unmanned aircraft systems. Stapp Car Crash J. 63, 29–64. https://doi.org/10.4271/2019-22-0002.
Sun, S., de Visser, C., 2019. Aerodynamic model identification of a quadrotor subjected to rotor failures in the high-speed flight regime. IEEE Rob. Autom. Lett. 4 (4), 3868–3875.
Sturdivan, L.M., Viano, D.C., Champion, H.R., 2004. Analysis of injury criteria to assess chest and abdominal injury risks in blunt and ballistic impacts. J. Trauma Acute Care Surg. 56 (3), 651–663.
Thums, 2018. Documentation Total Human Model for Safety (THUMS), AM50 pedestrian/occupant model academic version 4.02_20181226. Toyota Motor Corporation.
Tyrell, D.C., Severson, K.J., Marquis, B.P., 1995. Analysis of occupant protection strategies in train collisions. Crashworthiness and Occupant Protection in Transportation System, ASME AMD Vol 210/BED Vol 30,1995.
Viano, D.C., Lau, I.V., Ashbury, C., King, A.I., Begeman, P., 1989. Biomechanics of the human chest, abdomen and pelvis in lateral impact. Accid. Anal. Prev. 21, 553–574.
Washington, A., Clothier, R.A., Silva, J., 2017. A review of unmanned aircraft system ground risk models. Prog. Aerosp. Sci. 95, 24–44.
Weibel, R., Hansman, R.J., 2004. Safety considerations for operation of different classes of UAVs in the NAS. Unmanned Unlimited, Technical Conf., Workshop and Exhibit, 20-23 Sept. 2004, Chicago, IL, AIAA-2004-6421, pp. 1-11.
Weng, Y.B., Bian, K., Gunasekaran, J., Gholipour, C.V., Mao, H., 2021. Modelling small remotely piloted aircraft system to head impact for investigating craniocerebral response. J. Biomech. https://doi.org/10.1016/j.jbiomech.2021.110748.
Wing, 2023. Drone delivery, URL: https://wing.com/ [retrieved 20th, July 2023].
Zipline, 2023. Instant delivery & logistics, URL: https://www.flyzipline.com/ [retrieved 20th, July 2023].